

Structure of Boranes
Based on the Topology of
Molecular Electron Density

By

Naeyma Nahida Islam

A thesis submitted in partial fulfillment of the
requirements for the degree of
Master of Science in Chemistry
Middle Tennessee State University

August 2016

Thesis Committee:

Dr. Tibor Koritsanszky (Major Professor)

Dr. Keying Ding

Dr. Jing Kong

ACKNOWLEDGEMENTS

I would like to express my sincere gratitude to my advisor **Professor Dr. Tibor Koritsanszky** for the continuous support. His guidance helped me in my research and writing of my thesis.

I would also like to thank the rest of my thesis committee: Dr. Keiying Ding and Dr. Jing Kong.

Last, but not least, I would like to thank my lab-mates and my family.

ABSTRACT

The Quantum Theory of Atoms in Molecules (QTAIM) is utilized in this computational study to characterize the structure of some representative borane molecules (closo-, nido-, and arachno- boranes). Being connectivity-rich but electron-deficient, these molecules exhibit nontraditional bonding patterns whose adequate classification require nontraditional bonding concepts.

Multi-center Molecular Orbitals (MO), equilibrium nuclear geometries and normal modes of vibrations are derived at the B3LYP/cc-pVTZ level of theory using the Gaussian-09 program package. Both the static (stationary) and dynamic one-electron densities (EDs) are analysed to access QTAIM descriptors, such as the value of the ED, and its principal curvatures at all critical points, the bond-path length and the topological graph. In term of these figures, we characterize and compare atomic interactions found in borane molecules and establish their structural stability. We observe chemically equivalent bonds to exhibit similar topology. All but the terminal B-H bonds are at the borderline of shared and closed-shell interactions. Certain distance-based atom-atom contacts suggested by experimental structures are however absent in the topological structure, though good agreement is found between the experimental and calculated geometry. Investigations of the Laplacian of the ED, (that identifies regions of local charge concentrations / depletions), lead to a general conclusion that the stability of the boron framework (including B-H-B bridges) is mainly a consequence of electron delocalization over three- and four-membered rings

formed via weak bonds. In a cage or 'open-cage' type structure the delocalization appears to fuse rings together even though they do not share a common plane. This finding seems to support the intuitive concept of 3D aromaticity invoked on the basis of the localized-MO model used to describe the structure of polyhedral boranes.

The QTAIM identifies a stable structure with a set of equivalent topological graphs corresponding to different nuclear configurations in the neighborhood of the stationary one. A strong support for the stability of these borane structures is gained, for the first time, from showing that their static and dynamic (averaged over nuclear displacements of harmonic vibrations) EDs are indeed topologically equivalent.

TABLE OF CONTENTS

LIST OF TABLES	vi
LIST OF FIGURES	vii
1 INTRODUCTION	1
1.1 Boranes	1
1.1.1 Nomenclature	1
1.1.2 Early Structural Studies	1
1.1.3 Three - Center Bonds.....	4
1.1.4 Basic Assumptions ¹⁰	6
1.1.5 The Equation of Balance and STYX Numbers.....	7
1.1.6 Cluster Structure and Wade's Rule	9
1.1.6.1 Hydro Borane Clusters	9
1.1.6.2 Classification of Polyhedral Boranes.....	9
1.1.6.3 Wade's Rule.....	10
1.2 Static and Dynamic Electron Density	11
1.2.1 Computational Background ¹²	11
1.2.2 Computational Method	12
1.2.2.1 The Wave Function and its Electron Density	12
1.2.3 Computer Programs Used	16
1.3 The Quantum Theory of Atoms in Molecules (QTAIM)	17
1.3.1 Topological Atom and Atomic Properties	17
1.3.2 Critical Points	20
1.3.3 The Laplacian	23
1.3.4 Characterization of Bond Paths.....	24
2 OBJECTIVE	25
3 METHODS.....	25
4 RESULT AND DISCUSSION	27
5 CONCLUSION	70
REFERENCES	74
APPENDICES	81
APPENDIX A: ADDITIONAL TABLES	82

LIST OF TABLES

Table 1: Early structure of Boranes	2
Table 2: Total number of atomic orbitals and valence electrons in selected boranes	5
Table 3: STYX number for Boron Hydrides	8
Table 4: Number of SEPs offered for cluster bonding for different Boranes	10
Table 5: Different types of critical points in $\rho(\mathbf{r})^{38}$	21
Table 6: Comparison of relevant experimental and calculated geometrical parameters for B_2H_6	28
Table 7: Topological properties of B_2H_6	30
Table 8: Comparison of experimental and calculated geometries for B_5H_9	34
Table 9: Topological properties of B_5H_9	37
Table 10: Comparison of experimental ^{2, 34} and calculated geometries for B_6H_{10}	40
Table 11: Topological properties B_6H_{10} (C_s)	44
Table 12: Comparison of experimental and optimized geometries for $B_{10}H_{14}$	47
Table 13: Topological properties $B_{10}H_{14}$ (C_s)	49
Table 14: Comparison of experimental and calculated geometries for B_4H_{10}	54
Table 15: Topological properties B_4H_{10} (C_{2v})	56
Table 16: Comparison of experimental and calculated bond distances for $B_6H_6^{2-}$	59
Table 17: Topological properties of $B_6H_6^{2-}$ (Symmetry O_h)	61
Table 18: Topological Properties at of Static and Dynamic EDs. Comparison of ρ ($e/\text{\AA}^3$;), $\nabla^2\rho$ ($e/\text{\AA}^5$;) and λ_i ($e/\text{\AA}^5$;) in Boranes	65
Table A 1: B_2H_6 , D_{2h} , $E_e = -52.8414$ au. (Atomic coordinates are in atomic units)	82
Table A 2: B_5H_9 , C_{4v} , $E_e(A) = -128.632$ au. (Atomic coordinates are in atomic units) ..	82
Table A 3: B_6H_{10} , C_s , $E_e(A) = -153.9$ au. (Atomic coordinates are in atomic units).	83
Table A 4: B_6H_{14} , C_s , $E_e(A) = -257.081$ au. (Atomic coordinates are in atomic units) ...	83
Table A 5: B_4H_{10} , C_{2v} , $E_e = -104.525$ au. (Atomic coordinates are in atomic units)	84
Table A 6: $B_6H_6^{2-}$, O_h , $E_e(A) = -152.736$ au. (Atomic coordinates are in atomic units) ..	85

LIST OF FIGURES

Figure 1: The structure of B_2H_6	2
Figure 2: The structure of B_4H_{10}	2
Figure 3: The structure of B_5H_9	3
Figure 4: The structure of B_6H_{10}	3
Figure 5: The structure of $B_{10}H_{14}$	4
Figure 6: Bonding in Diborane.....	6
Figure 7: Example of three center bonds	7
Figure 8: Electron density $\rho(r)$ of C_3H_6 in the plane containing C-C-C (top) and equivalent gradient vector field (bottom) with the trajectories (bottom, red) which is vertical to the contour lines of $\rho(r)$	19
Figure 9: The IR structure of Diborane (B_2H_6).....	28
Figure 10: Molecular graphs for B_2H_6 with bond and ring critical points denoted by green and red dots respectively. Note the inwardly curved nature of the bond path linking the bridging protons.	31
Figure 11: Contour maps of the Laplacian of the electron density for B_2H_6 in the plane of B-H-B Bridge. The pink contour lines depict regions of local charge concentration (negative values) and blue line depict region of local charge depletion (positive value).....	32
Figure 12: Contour maps of the Laplacian of the electron density ($V^2 \rho_b$) for B_2H_6 in the plane of terminal hydrogen. The pink contour lines depict regions of local charge concentration (negative values) and blue line depict region of local charge depletion (positive value).....	32
Figure 13: The X-ray structure of B_5H_9	34
Figure 14: Molecular graphs for B_5H_9 with bond and ring critical points denoted by green and red dots respectively.....	37
Figure 15: Contour maps of the Laplacian distributions($V^2 \rho_b$) in the equatorial plane of B_5H_9 . The pink contour lines depict regions of local charge concentration (negative values) and blue line depict region of local charge depletion (positive value).	38
Figure 16: Contour maps of the Laplacian distributions($V^2 \rho_b$) for B_5H_9 in the plane containing $B_2-B_5-H_8-B_3$. The pink contour lines depict regions of local charge	

concentration (negative values) and blue line depict region of local charge depletion (positive value).....	39
Figure 17: The X-ray and microwave structure of B_6H_{10}	41
Figure 18: The topological graph for B_6H_{10} with bond and ring critical points denoted by blue and red dots respectively. The trajectories interconnecting the RCPs with the BCP's are not drawn for the lower half of the graph. Note the inwardly curved nature of the bond path linking the bridging protons.	43
Figure 19: Contour maps of the Laplacian distributions($V^2 \rho_b$) for B_6H_{10} in the plain containing $B_2-B_{10}-B_9$. It is seen that valence shell charge concentration (VSCC) is higher for B_9-B_{10} . The pink contour lines depict regions of local charge concentration (negative values) and green line depict region of local charge depletion (positive value).....	45
Figure 20: Contour maps of the Laplacian distributions($V^2 \rho_b$) for B_6H_{10} in plane of equatorial B-B bonds. Notations are the same as in Figure 19.....	46
Figure 21: The neutron diffraction structure of $B_{10}H_{14}$	47
Figure 22: Molecular graphs for $B_{10}H_{14}$ with bond and ring critical points denoted by blue and red dots respectively. Note the inwardly curved nature of the bond path linking the bridging protons.	51
Figure 23: Contour maps of the Laplacian distributions ($V^2 \rho_b$) for $B_{10}H_{14}$ in the plain defined by the $B_4-B_3-B_1$ ring. Pink (blue) contour lines represent negative (positive) values. It is seen that the VSCC is higher for B_1-B_4 bond	52
Figure 24: Contour maps of the Laplacian distributions($V^2 \rho_b$) for $B_{10}H_{14}$ in the plain containing $B_5-B_4-B_6$. The pink contour lines depict regions of local charge concentration (negative values) and blue line depict region of local charge depletion (positive value).....	53
Figure 25: The electron diffraction structure of B_4H_{10}	55
Figure 26: Molecular graphs for B_4H_{10} with bond and ring critical points denoted by blue and red dots respectively. Note the inwardly curved nature of the bond path linking the bridging protons.	57
Figure 27: Contour maps of the Laplacian distributions($V^2 \rho_b$) for B_4H_{10} in the plain containing $B_1-H_8-B_4-H_9-B_2$. The pink contour lines depict regions of local charge	

concentration (negative values) and blue line depict region of local charge depletion (positive value). It is seen that the VSCC is higher for B ₁ -H ₈ bond than that for B ₄ -H ₈ .	58
Figure 28: The electron diffraction structure of B ₆ H ₆ ²⁻	59
Figure 29: Molecular graphs for B ₆ H ₆ ²⁻ with bond, ring and cage critical points denoted by green, red and orange dots respectively.	61
Figure 30: Contour maps of the Laplacian distributions ($V^2 \rho_b$) for B ₆ H ₆ ²⁻ in the plain containing B ₄ -B ₅ -B ₆ . The pink contour lines depict regions of local charge concentration (negative values) and blue line depict region of local charge depletion (positive value).....	62
Figure 31: Change in the curvatures caused by thermal smearing calculated for the B ₁ -H ₂ bond path in B ₂ H ₆ . Each curve represents differences between dynamic and static properties as a function of distance from the B-atom: ($V^2 \rho$) _T - $V^2 \rho$ (Delta(L)), (λ_1) _T - λ_1 (Delta(L1)) and (λ_3) _T - λ_3 (Delta(L3))	66
Figure 32: Change in the curvatures caused by thermal smearing calculated along the axis of the bridging H-atoms (H ₂ ...H ₃) in B ₂ H ₆ . Notations are the same as in Figure 31.	67
Figure 33: Change in the curvatures caused by thermal smearing calculated along the terminal B ₁ -H ₇ bond in B ₂ H ₆ . Notations are the same as in Figure 31.	68
Figure 34: Contour map of change in the Laplacian distribution caused by thermal smearing calculated for the B-H _b -B bond path in B ₂ H ₆	69

1 INTRODUCTION

1.1 BORANES

Boranes, also known as boron hydrides, consist of a big group of compounds with the general molecular formula of B_xH_y . Because of their electron deficient nature, bonding in boranes have been at the focus of theoretical-chemistry research during the past few decades.

1.1.1 Nomenclature

The neutral boranes is named by the number of boron atoms which is provided by a prefix and by the number of hydrogen atoms which is provided in parentheses behind the name.

Example: $B_5H_9 \rightarrow$ Pentaborane (9)¹, $B_4H_{10} \rightarrow$ tetraborane (10)

1.1.2 Early Structural Studies

The experimentally characterized boranes are: B_2H_6 ², B_4H_{10} ^{4,5}, B_6H_{10} , B_5H_9 ^{6,7}, B_9H_{15} ², $B_{10}H_{14}$ ⁹, B_5H_{11} ², and $B_{18}H_{22}$ ².

Table I: Early structure of Boranes

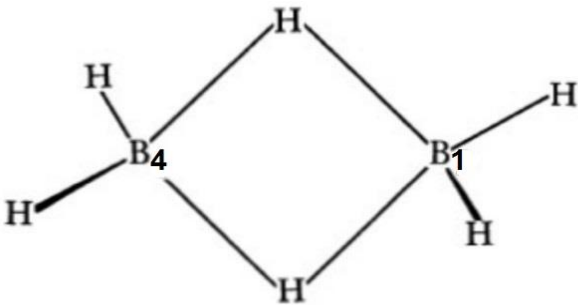
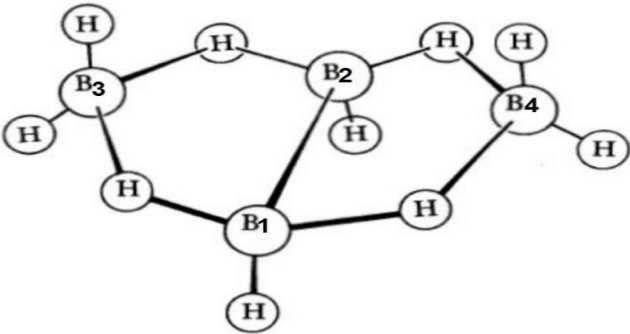
Structure	Molecules
 <p>Figure 1: The structure of B_2H_6</p> <p>The B_1-B_4 distance is 1.77 Å, the B-H distance is 1.19 Å, the B-H_b(bridge) distance is 1.33 Å, and the H_bH angle is 121.5°².</p>	<p>B_2H_6:</p> <p>The bridge type structure, generally recognized to have been proven by Price⁵⁴ on the basis of infrared spectroscopy, is the correct one for diborane.</p> <p>It was first suggested by Diltney³</p>
 <p>Figure 2: The structure of B_4H_{10}.</p> <p>The B_1-B_2 distance is 1.71 Å, and the other four close B...B distances are 1.84 Å. The B-H distances average to 1.19 Å, while the B-H_b(bridge) distances are 1.33 Å towards B_2 and B_1 and 1.43 Å toward B_4 and $B_3$².</p>	<p>B_4H_{10}:</p> <p>The crystallographic atomic positions were unambiguously established by an X-ray diffraction study^{4,5}.</p>

Table 1 (cont.)

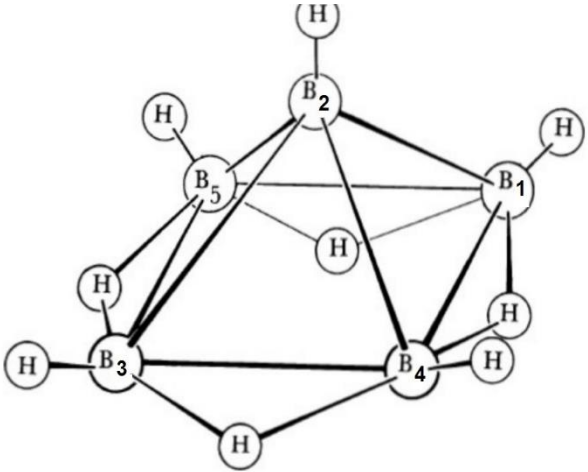
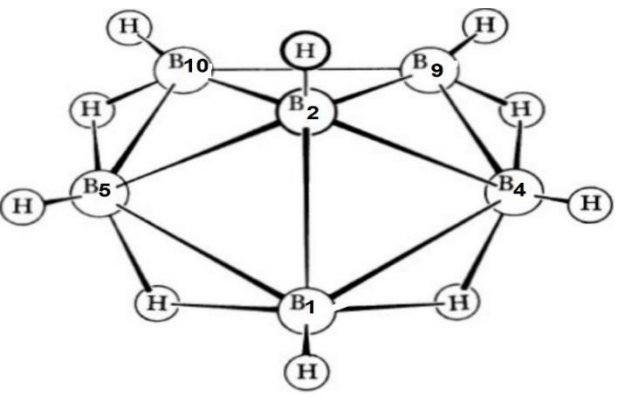
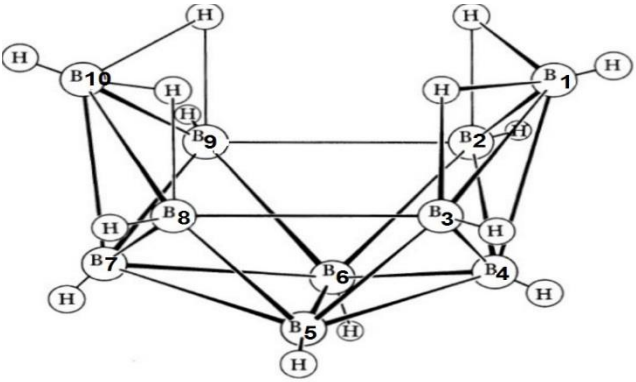
Structure	Molecules
 <p>Figure 3: The structure of B_5H_9.</p> <p>The close B-B distances to B_2 are 1.69 Å, and those among atoms 1, 3, 4 and 5 are 1.80 Å.²</p>	<p>The certainty of this structure is based on the crystal –structure study^{6,7}. The borane arrangement is closely related to the octahedron which is found in the cubic borides⁸.</p>
 <p>Figure 4: The structure of B_6H_{10}.</p> <p>The B-B distances are 1.74 Å for 2-1, 1.79 Å for 1-4 and 1-5, 1.75 Å for 2-4 and 2-5, 1.80 Å for 2-9 and 2-10, 1.74 Å for 9-4 and 5-10, and interestingly 1.60 Å for 9-10, the shortest observed distances among the boron hydrides.²</p>	<p>B_6H_{10}:</p> <p>The structure of B_6H_{10}^{61, 62, 63} has six B atoms from the icosahedral arrangement where each is bonded to one terminal H atom. There are also 4 bridge hydrogen atoms.</p>

Table 1 (cont.)

Structure	Molecules
 <p>Figure 5: The structure of $B_{10}H_{14}$.</p> <p>The B-B bond distances are 1.71 Å for 5-6; 1.80 Å for 6-4 and 5-7; 1.78 Å for 4-5 and 6-7; 1.76 Å for 4-2 and 7-8; 1.80 Å for 4-3 and 7-9; 1.77 Å for 2-1, 1-3, 8-10, and 9-10; 1.72 Å for 4-1 and 7-10; 1.78 Å for 6-2 and 5-8; 1.77 Å for 5-3 and 6-9 ; and interestingly 2.01 Å for 2-9 and 3-8.²</p>	<p>$B_{10}H_{14}$:</p> <p>The molecular structure of decaborane has been uniquely established by an X-ray diffraction study⁹.</p>

1.1.3 Three - Center Bonds

The three-center bond introduced to describe the bonding situation in borane structures was a new concept of the traditional localized Molecular Orbital (MO) model, within which 'the normal covalent' interaction is considered to be a two-center bond²; the mixing of two atomic orbitals (one centered on each atom) yields the formation of one bonding and one antibonding MO, the former being double-occupied. Analogously, three atoms may give three orbitals whose

combination produces one bonding and two antibonding MOs; two electrons occupy the former to make a three-center bond.

In modeling electron deficient molecules like boranes, for which there are more ‘available’ atomic orbitals (close in energy) than valence electrons, the application of the concept of three-center, two-electron bond (3c-2e) turned out to be highly beneficial.

Table 2: Total number of atomic orbitals and valence electrons in selected boranes

Hydrides	Number of Atomic Orbitals	Numbers of Valence shell Electrons	‘Excess’ Orbitals
B_2H_6	14	12	2
B_4H_{10}	26	22	4
B_5H_9	29	24	5
$B_{10}H_{14}$	54	44	10

1.1.4 Basic Assumptions¹⁰

1. Taking B_2H_6 as an example, only the $1s$ orbital of hydrogen and the four sp^3 orbitals of boron are used (Figure 6). The hydrogen orbital, one hybridized B orbital, and one electron from each atom are required to form a terminal $B-H_t$ bond considered as a “normal”, localized, single bond. These bonds are expected to be nonpolar due to very small difference in electronegativity of hydrogen and boron.

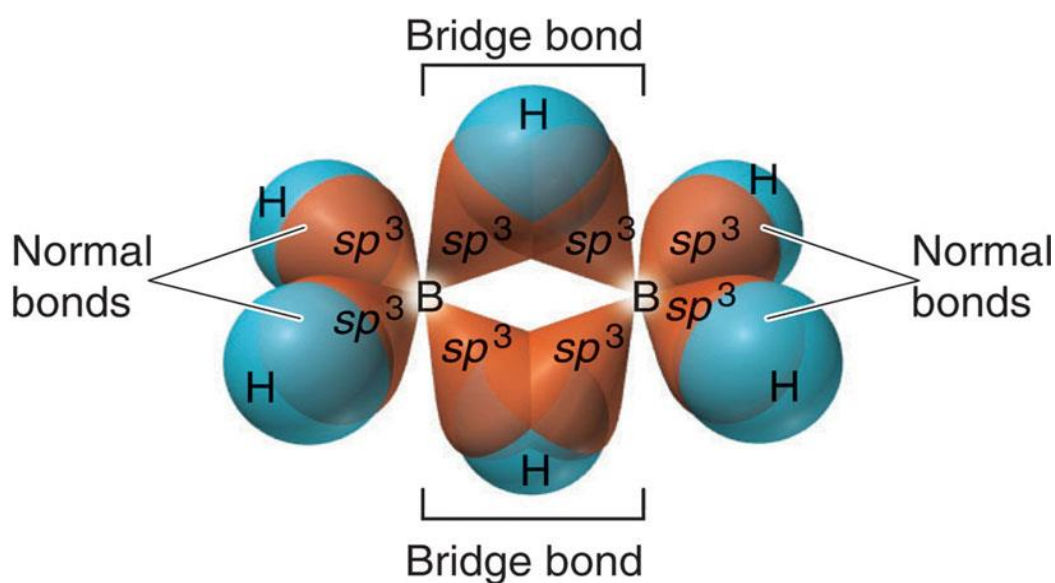


Figure 6: Bonding in Diborane

- The 1s orbital of the bridging H-atom (H_b) and one hybrid orbital from each B atom are required for each B- H_b -B bridge bond (Figure 7a) considered as a filled ($3c-2e$) localized bonding MO.

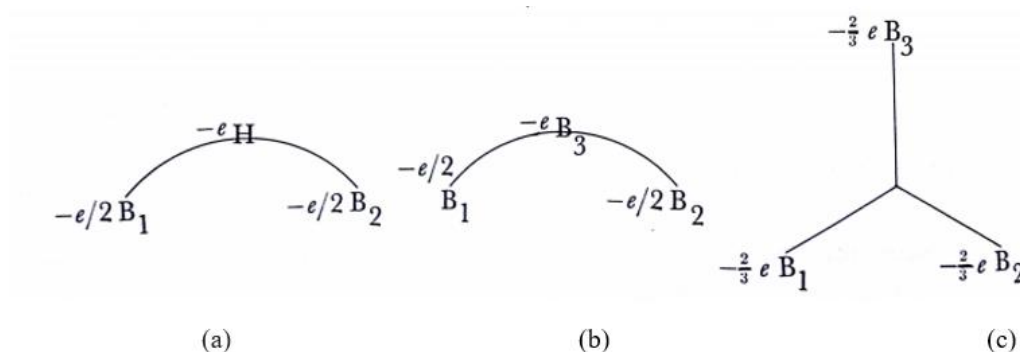


Figure 7: Example of three center bonds

- The orbitals and electrons of any particular B-atom are distributed so as to meet the requirements of the external B- H_t single bonds and the bridge B- H_b -B bonds. The remaining orbitals and electrons are then used for the framework MOs.
- The framework MOs are formed from B-hybrid orbitals as dictated by the local connectivity and/or symmetry of each atom.

1.1.5 The Equation of Balance and STYX Numbers

The numbers of orbitals, electrons, H and B atoms, and bonds of several types, can easily be coded¹⁰, as follows:

For a boron hydride, B_pH_{p+q} ,

S = Number of B-H_b-B bridges

T = Number of B-B_b-B bridges

Y = Number of B-B single bonds

X = Number of extra B-H groups

The H-atom balance is: $S+X = q$.²

The total number of three-center bonds is the same as the number of B atoms ($S+T = p$), because each B atom provides four orbitals but only three electrons.

Furthermore, if we consider 'B-H' as the bonding unit (each 'consuming' one electron pair), the p electron pairs are used by the three-center B-B_b-B and two-center B-B bonds, so that $p = T+Y+q/2$.

Table 3: STYX number for Boron Hydrides

$B_nH_{(n+q)}$	S (B-H-B)	T (B-B-B)	Y (B-B)	X (BH ₂)
B ₂ H ₆	2	0	0	2
B ₄ H ₁₀	4	0	1	2
B ₅ H ₉	4	1	2	0
B ₅ H ₁₁	3	2	0	3
B ₆ H ₁₀	4	2	2	0
B ₁₀ H ₁₄	4	6	2	0

1.1.6 Cluster Structure and Wade's Rule

1.1.6.1 Hydro Borane Clusters

The structure of boranes are often characterised as a polyhedral or deltahedra; the former has triangular faces, while in the latter, one or more vertices of the triangle are missing. These molecules exhibit cage or cage-type structures .

1.1.6.2 Classification of Polyhedral Boranes

- a) Closo-borane: it is a complete, closed polyhedral cluster of n B-atoms.
Example: $B_6H_6^{2-}$ is closo type with the 6 B-atoms situated at the corners of an octahedron.
- b) Nido-boranes: it is an open structure in which the n B-atoms occupy the n corners of an (n+1)-cornered polyhedron. Example: B_5H_9 where 5 B-atoms lie at the corners of a square pyramid missing one corner. The other examples are: B_2H_6 , B_6H_{10} , $B_{10}H_{14}$.
- c) Arachno-boranes: it is an more open cluster where the B-atoms occupy n attached corners of an (n+2) – cornered polyhedron. Example: B_4H_{10} in which the 4 B-atoms lie at the corners of an octahedron missing two corners.

1.1.6.3 Wade's Rule

Wade's rules¹¹ make it easy to apprehend structural relationship of various boranes. It is an electron counting scheme to derive the number of skeletal electron pairs (SEP) offered for cluster bonding, as follows:

- Count the number of B-H units,
- Each B-H unit contains a total of 4 valence electrons. Since two of these electrons are essential to form the bond between B and H, each B-H unit provides one SEP,
- Every additional H-atom gives one skeletal electron,
- Any extra charge (overall charge of the molecule) also contributes to the SEPs,
- Obviously, to obtain the total number of SEPs, the resulting number of electrons has to be divided by two. The general structure is expressed by the number of SEPs.

Table 4: Number of SEPs offered for cluster bonding for different Boranes

Formula	SEPs	Class	Example
$[B_nH_n]^{2-}$	$n+1$	closo	$B_6H_6^{2-}$
B_nH_{n+4}	$n+2$	nido	B_2H_6 , B_5H_9 , B_6H_{10}
B_nH_{n+6}	$n+3$	arachno	B_4H_{10}

1.2 STATIC AND DYNAMIC ELECTRON DENSITY

1.2.1 Computational Background¹²

The static Electron Density (ρ , ED) of a chemical scheme is a probability density function (PDF) which gives the probability of finding any electron in an infinitesimal volume element of the 3D space for a static (fixed) nuclear configuration. It can be derived from the wave function (WF) by summing the square of the probability amplitude with respect to all spin coordinates and integrating it with respect to all but one electronic spatial variables. It is a 3D marginal distribution that integrates to the total number of electrons.

By exploring the topology of ED, it is possible to unambiguously define many static and sensitive properties of a molecule. Through a topological analysis of this scalar field (as detailed below), basic concepts of chemistry such as bonding, stability and even the very definition of an 'atom in a molecule' can be quantitatively described. Properties of distinct molecules are not directly observable through experiments (such as an atom in a molecule, though both of these concepts have enjoyed fundamental operative power for centuries). As we know, an atom consists of negatively charged electrons and a positively charged nucleus. According to the laws of quantum mechanics (QM), a molecule composed of more than one atom bound together by balanced electrostatic forces possesses internal degrees of freedom, both electronic and nuclear. The latter modes are identified as molecular vibrations.

1.2.2 Computational Method

1.2.2.1 The Wave Function and its Electron Density

One can attempt to model either the electronic WF, or the ED to estimate molecular properties. These two functions are linked in density functional theory (DFT), on the basis of the Hohenberg-Kohn (HK) theorem establishing the existence of a unique functional relationship between the two¹⁴ (and between the energy and the ED).

1.2.2.1.1 Density-Functional Theory

So far it has been impossible to obtain exact functionals for the electronic kinetic ($T[\rho]$) and exchange-correlation energies ($E_{xc}[\rho]$). In the expression below only the $V_{ne}[\rho]$ (electronic-nuclear Coulomb potential) and the $J[\rho]$ (electron-electron Coulomb potential) terms are known:

$$E[\rho] = T[\rho] + V_{ne}[\rho] + J[\rho] + E_{xc}[\rho] \quad \text{Eq. 6}$$

A technical bypass of these issues is provided by the Kohn-Sham scheme¹⁵ (KS) that expresses the density in terms of a Slater determinant of one-electron orbitals of the non-interacting system for which $T[\rho]$ is known. This is equivalent to assuming the ED of the interacting system to be replaceable by the ED of a hypothetical non-interacting system and that the corresponding corrections can be 'built' into the unknown E_{xc} term. To make this formalism 'work',

various approximations to E_{XC} have been developed, and some of these approximate functionals are capable of yielding better results than Hartree-Fock (HF) theory¹³ due to the (albeit approximate) inclusion of electronic correlation.

The Hybrid Functional, B3LYP

Hybrid functionals, one of the type of approximations to the E_{XC} , include a part of the HF exchange supplemented by exchange and correlation terms from other sources (*ab initio* or empirical). The B3LYP functional (Becke, 3-parameter, Lee-Yang-Parr)^{16, 17} is one of the most commonly used:

$$E_{xc}^{B3LYP} = E_x^{LDA} + a_0(E_x^{HF} - E_x^{LDA}) + a_x(E_x^{GGA} - E_x^{LDA}) + E_c^{LDA} + a_c(E_c^{GGA} - E_c^{LDA})$$

Eq. 10

with the parameters (a_0, a_x, a_c) derived by fitting the results of post-HF calculations. The E_x^{GGA} and E_c^{GGA} terms are based on the generalized gradient approximations: the Becke-88 exchange functional¹⁸ and the correlation functional of Lee, Yang and Parr¹⁹, while E_c^{LDA} is from the VWN local-density calculation to the correlation functional²⁰.

1.2.2.1.2 Basis Sets

All *ab-initio* QC calculations require the definition of the basis set (a set of functions, called basis functions or ‘primitives’) which are linearly combined to create MOs. Typically, only nucleus-centered and Gaussian-type basis functions are used nowadays.

Correlation-consistent basis sets:

The widely used correlation-consistent (cc) basis sets are planned so as to give molecular electronic energies converging to that achievable at the complete-basis-set (CBS), by means of empirical extrapolation methods. The basis sets developed in such a way for the first- and second-row atoms are designated as cc-pVNZ where N = D, T, Q, 5, ... (D = double, T = triple, etc.). The 'cc-p', means 'correlation-consistent polarized' and the 'V' stands for valence-only basis sets. In this work we used the cc-pVTZ (triple-zeta, contracted) basis.

1.2.2.1.3 Dynamic molecular ED

In the LCAO-MO and harmonic-convolution approximations, analytic evaluation of the dynamic (thermally smeared) ED involves allocating vibrational PDFs to the two-center products of Gaussian basis functions from the knowledge of PDFs for the nuclei²². Thus the dynamic ED, using this 'riding' model, can be derived from the stationary ED (corresponding to the equilibrium nuclear configuration), if the harmonic frequencies and normal modes are available. The calculation leads to the canonical-ensemble average (the molecule being in thermal equilibrium with the rest of the system) that agrees well with the statistical average taken over a population of static EDs calculated for geometries consistent with nuclear displacements due to vibrations.

1.2.2.1.4 Geometry Optimization

Geometry optimization is an important computational method to estimate the equilibrium molecular geometry¹³. It is to locate the minimum of the Born-Oppenheimer (BO) electronic energy as an approximate parametric function of the nuclear positions, starting from an initial geometry. The method involves calculating the actual forces acting on each nucleus and adjusting the positions accordingly, until all forces vanish. The procedure is iterative but self-consistent.

1.2.2.1.5 Vibrational Frequency Calculation

Assuming that the BO-energy at the minimum is a quadratic function of small nuclear displacements relative to the stationary geometry, harmonic vibration frequencies and normal modes can be obtained. Since the global minimum is not ensured by the geometry optimization, all frequencies obtained must be checked if they are positive (real-valued), otherwise the optimization is settled at a saddle point (transition structure). An additional test explores the lowest-frequency modes that should be as close to zero (in frequency) as possible, if the optimization was done in redundant coordinates (most commonly in a Cartesian frame). We used the 'very tight' condition for the Gaussin-09 calculations to ensure that the external modes (3 translations and 3 rotations) are indeed 'removed' from the $(3N-6)$ internal modes. In summary, we are confident that all structures discussed in this thesis correspond to a minimum (though not necessarily the global minimum) of the BO electronic energy hypersurface and

thus they represent quantum chemically stable structures (though not necessarily the most stable ones).

1.2.3 Computer Programs Used

Gaussian-09

From empirically parameterized molecular mechanics methods to the most advanced configuration interaction and coupled-cluster methods, the Gaussian package provides a full capability to perform different types of molecular or solid-state electronic structure calculation²¹.

Due to the popularity and longevity of Gaussian-type functions used for QM calculation, many post-processing analysis codes are able to handle Gaussian outputs.

Denprop²³

Denprop is such a post-processing code²³ developed locally by the computational group of our Department. Its functionality includes the topological analyses of theoretical static, dynamic and experimental EDs²³.

AIMAll

AIMAll²⁴ is a package specifically used for performing QTAIM analyses of EDs based on Gaussian WFs. Its capability is limited to static properties.

1.3 THE QUANTUM THEORY OF ATOMS IN MOLECULES (QTAIM)

The QTAIM developed by Richard Bader²⁵ is an explanatory theory which intends to recover chemical insight from modern high resolution electron densities²⁶. These densities may be derived either experimentally or from or *ab initio* calculations. The theory makes it possible to define important concepts of chemistry: the atom, chemical bonding and thus the molecule. Currently, QTAIM is used in many different areas of research including surface science²⁷, solid state physics²⁸, biological chemistry²⁹, organometallic chemistry³⁰, noble gas chemistry³¹, physical organic chemistry³², transition metal complex chemistry³³, boron chemistry³⁴, lithium chemistry³⁵ and others.

1.3.1 Topological Atom and Atomic Properties

Topology is the study of geometrical properties and their spatial relationships that are invariant upon changing the shape and size of objects involved. The topological analysis of the ED ($\rho(\mathbf{r})$) is about exploring its gradient vector field $\nabla\rho(\mathbf{r})$, that is, tracing its gradient trajectories and finding its critical points (where

$\nabla\rho(\mathbf{r})=0$) and their characteristics. All these topological properties play a special role in characterizing a molecular structure.

The gradient of $\rho(\mathbf{r})$ is a vector field,

$$\nabla\rho(\mathbf{r}) = \mathbf{i} \partial\rho(\mathbf{r})/\partial x + \mathbf{j} \partial\rho(\mathbf{r})/\partial y + \mathbf{k} \partial\rho(\mathbf{r})/\partial z \quad \text{Eq. 11}$$

where, \mathbf{i} , \mathbf{j} , \mathbf{k} represent the element vectors of a cartesian coordinate system. A gradient path (a trajectory) is all the time perpendicular to the contour lines of $\rho(\mathbf{r})$ (the constant-density lines) and terminates the highest increase in $\rho(\mathbf{r})$ (Figure 8). All gradient paths terminating at a maximum belong to the same basin, which is considered to be an atom in molecule (a nuclear attractor). This basin is defined by closed surfaces not crossed by trajectories originating at infinity:

$$\nabla\rho(\mathbf{r}) \cdot \mathbf{n}(\mathbf{r}) = 0 \quad \text{Eq. 12}$$

where $\mathbf{n}(\mathbf{r})$ is the normal vector to the surface. These zero flux surfaces define the 3D domain (Ω) of atoms.

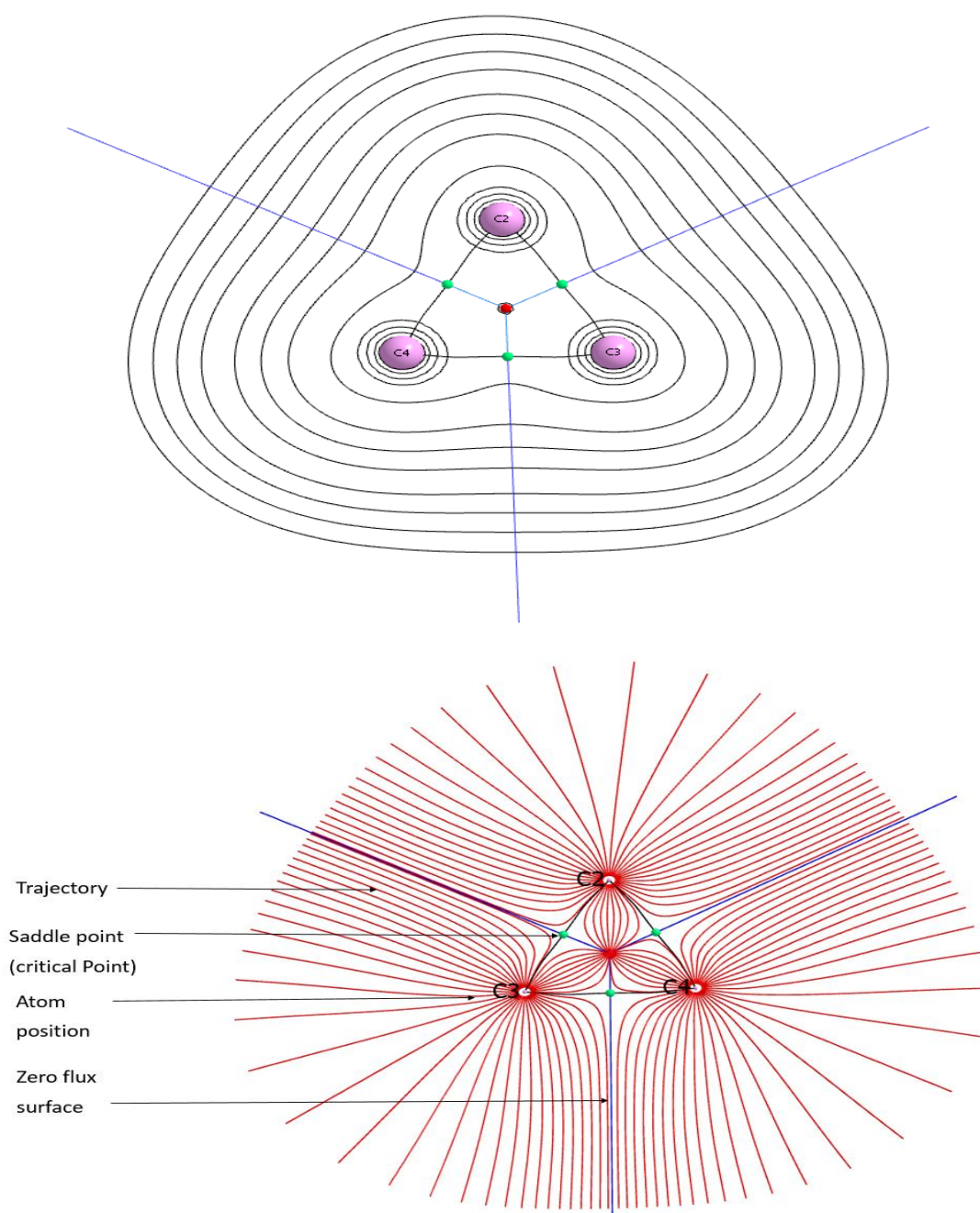


Figure 8: Electron density $\rho(r)$ of C_3H_6 in the plane containing C-C-C (top) and equivalent gradient vector field (bottom) with the trajectories (bottom, red) which is vertical to the contour lines of $\rho(r)$.

An integration of the ED over the volume of the atomic basin gives the topological charge of the atom. Since this charge encompasses all influential effects (polarization and charge transfer), it is usually quite different from those obtained by different WF-based partitioning methods^{36, 37}. We note that all properties of an atom in a molecule can be obtained by integrating the QM-based expressions over the atomic basin.

1.3.2 Critical Points

An important element of QTAIM is the critical point (CP). The starting and finishing points of a trajectory are extreme values in $\rho(\mathbf{r})$. These extrema (maxima, saddle or minima in the ED) are defined by the vanishing gradient of $\rho(\mathbf{r})$. The CPs can be classified with the help of the second derivatives of the ED at the CP. Diagonalization of the Hessian matrix formed by the six second derivatives of $\rho(\mathbf{r})$ taken at the CP,

$$H(\mathbf{r}) = \begin{bmatrix} \frac{\partial^2 \rho(\mathbf{r})}{\partial^2 x^2} & \frac{\partial^2 \rho(\mathbf{r})}{\partial x \partial y} & \frac{\partial^2 \rho(\mathbf{r})}{\partial x \partial z} \\ \frac{\partial^2 \rho(\mathbf{r})}{\partial y \partial x} & \frac{\partial^2 \rho(\mathbf{r})}{\partial^2 y^2} & \frac{\partial^2 \rho(\mathbf{r})}{\partial y \partial z} \\ \frac{\partial^2 \rho(\mathbf{r})}{\partial z \partial x} & \frac{\partial^2 \rho(\mathbf{r})}{\partial z \partial y} & \frac{\partial^2 \rho(\mathbf{r})}{\partial^2 z^2} \end{bmatrix} \quad \text{Eq. 13}$$

yields its three eigenvalues $\lambda_1, \lambda_2, \lambda_3$ (with $\lambda_1 \leq \lambda_2 \leq \lambda_3$), the principal curvatures of the ED associated with the corresponding eigenvectors.

A CP in $\rho(\mathbf{r})$ is characterized through the rank m (the number of non-zero eigenvalues λ_i) and the signature n (the algebraic sum of the signs of the eigenvalues). Only four types of CPs (m,n) are possible for a rank $m = 3$ (Table 5).

Table 5: Different types of critical points in $\rho(\mathbf{r})$ ³⁸

(m,n)	Topology in $\rho(\mathbf{r})$	λ_i	Explanation	Name
(3,-3)	Maximum in all direction	All $\lambda_i < 0$	The position of atom	Nuclear attractor critical point (NAP)
(3,-1)	Minimum in one directions ,Maximum in two direction	One $\lambda_i > 0$ Two $\lambda_i < 0$	Chemical bond	Bond critical point (BCP)
(3,+1)	Minimum in two direction, Maximum in one direction	Two $\lambda_i > 0$ One $\lambda_i < 0$	Middle of a ring of bonded atoms	Ring critical point (RCP)
(3,+3)	Minimum in all direction	All $\lambda_i > 0$	Middle of a cube of bonded atoms	Cage critical points (CCP)

Starting from a (3,-3)CP (a local maximum), the density decreases in all directions and thus the curvatures are negative. These local maxima in the ED are assigned to the nuclear positions (the CP is said to be a nuclear attractor).

There are two types of saddle points. At the (3,-1)CP (bond CP; BCP) the ED exhibits a minimum along the bond axis and it takes its maximum values along the two perpendicular directions (normal to the bond axis). The trajectories that originate at the BCP and terminate at one of the (3,-3) CPs define an interaction line, the bond path (BP) for the stationary geometry, along which the ED is maximum with respect to any other paths interconnecting the nuclei. The presence of a BCP and its related BP is a required and adequate condition for a chemical bond^{39, 40}. The other saddle point is a (3,+1) CP (two positive and one negative eigenvalues) where the density is minimum in two directions (in the plane defined by the two eigenvectors) and falls perpendicular to this plane. This CP is created in the middle of ring systems and so it is called the ring critical point (RCP). In the middle of a cage structure, $\rho(\mathbf{r})$ has a local minimum (where all three eigenvalues are positive). Therefore, a (3,+3) CP is called the cage critical points (CCP).

The number of different CPs found in a structure must satisfy the Poincare-Hopf equation^{41, 42}:

$$n_{NAP} - n_{BCP} - n_{RCP} - n_{CCP} = 1 \quad \text{Eq. 1}$$

1.3.3 The Laplacian

Since in the vicinity of the nuclei the distribution of the core electrons dominates the topology of the total ED, it is difficult to detect valence electron distributions due bonding or lone-pairs. Small changes in the topology of the ED are however illuminated in the Laplacian ($\nabla^2\rho$), the trace of the HESSIAN matrix.

$$\nabla^2\rho(r) = \frac{\partial^2\rho(r)}{\partial x^2} + \frac{\partial^2\rho(r)}{\partial y^2} + \frac{\partial^2\rho(r)}{\partial z^2} = \lambda_1 + \lambda_2 + \lambda_3 \quad \text{Eq. 16}$$

The Laplacian thus shows whether electronic charge is locally concentrated ($\nabla^2\rho(r) < 0$) or depleted ($\nabla^2\rho(r) > 0$). Maxima in the negative Laplacian, ((3,-3) CPs in $-\nabla^2\rho(r)$), thus shows local charge concentration which is termed VSCCs (valence shell charge concentrations). These concentrations pinpoint either bonding or non-bonding electron pairs⁴³. The spatial arrangement of the VSCCs are thus informative of the local bonding situation of an atom⁴⁴⁻⁴⁷ and is in agreement with the prediction of the VSRP theory⁴⁸⁻⁵¹. Covalent bonds can be identified by the overlapping of the VSCCs of the atoms, yielding accumulation of charge ($\nabla^2\rho(r_{BCP}) < 0$) in the bonding region. For this reason, covalent bonds are also known as shared interactions. When the bond is covalent but very polar, the BCP is moved to the less electronegative atom.

An alliance of the VSCCs of the bonding partners are not found for ionic bonds. In this case, there is a charge reduction at the electropositive atom and a charge accumulation at the electronegative atom. Since for the former atom ($\nabla^2\rho(r) >$

0), the BCP is shifted towards the charge depletion. Only one VSCC is noticeable which is ascribed to the electronegative atom. Because of the absence of overlap of the bonding VSCCs, the ionic bond is called a closed-shell interaction.

1.3.4 Characterization of Bond Paths

Since the BP does not necessarily coincide with the internuclear axis (unless dictated by symmetry), its length (BPL; R_b) is usually longer than the internuclear distance (R_e). In molecules which are electron deficient such as the boranes, the BPs linking bridging hydrogens are strongly bent towards the interior of the ring so as to maximize the binding from a minimum amount of ED⁵². When the magnitude of λ_2 is the smallest, then the quantity $\varepsilon = \left[\lambda_1 / \lambda_2 - 1 \right]$, the ellipticity⁵² of the bond, is indicative of the level to which the density is accumulated in a certain plane. The proximity of the ring and bond CPs, due to the relatively large bond ellipticity, plays an important role in the reactivity of molecules containing a three-membered ring⁵².

2 OBJECTIVE

The goal of this thesis research is a detailed characterization of the molecular structure of boranes on the basis of the QTAIM. In particular, we aim to see how traditional bonding concepts based on the strictly localized-MO model manifest themselves in the topology of the ED derived within the multicenter-MO model for the stationary nuclear configuration. The QTAIM-based analysis is especially suited for this purpose, since it is model independent (it operates on the ED rather than on the MOs) and conceptually simple. Most importantly, we want to elaborate on the thermodynamic stability of these molecules by the QTAIM analysis of their dynamic EDs smeared by nuclear vibrations.

3 METHODS

All QC calculations were performed by the Gaussian09⁵³ program suite using the B3LYP/cc-pVTZ level of theory. Topological analyses of the static EDs were done using the DENPROP²³ and AIMAll computer programs.

The normal mode analysis of an N -atom molecule allows the derivation of the $3N$ -multivariate normal distribution of nuclear displacements relative to their equilibrium positions ($u = R - R^0$)²² :

$$p(\mathbf{u}) = (2\pi)^{-\frac{2n}{2}} |\mathbf{U}|^{-\frac{1}{2}} \text{Exp} \left[-\frac{1}{2} \mathbf{u} \mathbf{U}^{-1} \overline{\mathbf{u}} \right] \quad \text{Eq. 17}$$

where \bar{u} represents the transpose of u and the covariance matrix is the Mean-Square Displacement Amplitude (MSDA) matrix (U) given by the expectation values of Cartesian nuclear displacement products (second moments):

$$U = \langle \bar{u}u \rangle_T \quad \text{Eq. 18}$$

The MSDAs are temperature dependent through the eigenvalues of U ($\delta = (\delta_{i=1,3 N})$):²²

$$U = L\delta\bar{L} \quad \text{Eq. 19}$$

$$\delta_j = \frac{h}{8\pi^2\nu_j} \coth\left(\frac{h\nu_j}{2k_B T}\right) \quad \text{Eq. 20}$$

where ν_j denotes the frequency of the j^{th} normal mode and L is the eigenvector matrix^{54, 55}.

A tri-variate normal distribution of a given nuclear center (a marginal PDF; P_a) smears the density units centered on that nucleus ($\rho_a(r_a), r_a = r - R_a$)³¹. This means that the 3N-multivariable normal distribution is taken as a product of N tri-variate normal distributions, giving rise to the one-center smeared ED.

$$\langle \rho(r) \rangle_T = \sum_a \int_{-\infty}^{\infty} \rho_a(r_a - u) P_a(u) du \quad \text{Eq. 21}$$

Since the two-center density units (Gaussian basis-products) ‘ride’ on two nuclear centers, their smearing must be evaluated with the correlated nuclear PDFs, that can also be done analytically. This formalism is implemented in the current version of the Denprop software package.

4 RESULT AND DISCUSSION

The collection of BPs²⁵ defines the topological graph (TG) for a given nuclear geometry and all geometries possessing equivalent molecular graphs possess the same molecular structure.^{62,25}

Structure of Nido-Boranes

Diborane, B₂H₆

The QC calculation was started with the experimental nuclear positions. The electronic energy and the optimized atomic coordinates of B₂H₆ are given in the appendix (Table A1).

Experimental and theoretical geometries of B₂H₆

The fascinating bridge-type structure for diborane (Figure 9) was proved by Price⁵⁶ based on electron diffraction data. The molecule possesses D_{2h} symmetry and contains four terminals and two bridging hydrogen atoms⁵⁷.

The experimentally determined geometrical parameters (IR and microwave) are compared with those calculated in this work in Table (6), showing that the B3LYP/cc-pVTZ optimized geometry of B₂H₆ is in a good agreement with the experimental results^{34, 66}.

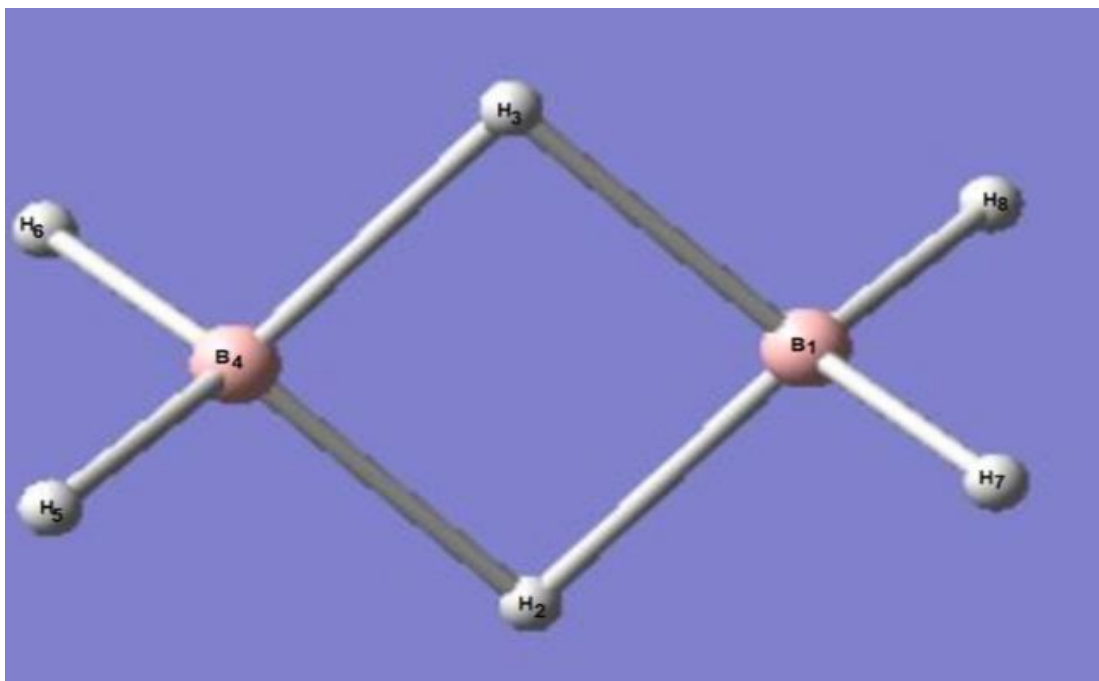


Figure 9: The IR structure of Diborane (B_2H_6)

Table 6: Comparison of relevant experimental and calculated geometrical parameters for B_2H_6

Bond distances/angles	Experimental	B3LYP/cc-pVTZ
B_1-B_4	1.743 \AA^{84}	1.758 \AA
B_4-H_5 (terminal)	1.184 \AA^{49}	1.185 \AA
B_1-H_2 (bridge)	1.314 \AA^{84}	1.312 \AA
$H_6-B_4-H_5$	121.5°^{49}	121.657°
$H_2-B_4-H_3$	96.9°^{49}	95.851°

Noticeable structural features are: elongated B-B distance; $d(B-H_t) < d(B-H_b)$ and $(H_t-B-H_t) > (H_b-B-H_b)$.

Topological analysis of the electron density of B₂H₆

The ED topology of the diborane molecule, as revealed by the HF method, is exhaustingly discussed in the literature³⁴. Since our results obtained at the BLYP/cc-PVTZ level (that empirically includes electron correlation) reproduce earlier observations, we only summarize the main conclusions.

According to the TG (Figure 10), each B-atom is bonded (interconnected via a BP) to two terminals and two bridge H-atoms. The bond topological indices reveal that the B-H_t interaction is more of a shared-type (covalent; $\nabla^2_{\rho_b} < 0$) than the B-H_b (closed-shell; $\nabla^2_{\rho_b} > 0$). Furthermore, for the latter bonds inwardly curved BPs are found ($\text{BPL}(\text{B-H}_b) > d(\text{B-H}_b)$). Most importantly, there is no BP interconnecting the two boron atoms. These findings are in qualitative accord with the classical localized-MO picture that suggests the presence of four traditional (2c-2e) B-H_t bonds and two weak (3c-2e) B-H_b-B bonds (STYX = 2002). A significant feature of the topology is the presence of an RCP (3+1) (located at the molecular center) corresponding to the B-H_b-B-H_b four membered ring. At this CP the density exhibits a saddle point; minimum in the plane of the H₂B-BH₂ framework but maximum normal to it in the other symmetry plane. This feature suggests two fused (3c-2e) bonds, or rather, a (4c-2e) delocalized bonding. The Laplacian contour maps plotted for the two symmetry planes (Figure 11 and Figure 12) show that the accumulation of negative charge between the B-atoms, and more prominently between the bridge

H-atoms, keeps the BH₂ units together. Since the charge accumulation / depletion is localized within the basin of the H_t / B atom, the B-H_t bond is not a typical shared interaction, yet it has more covalent character than the B-H_b bond.

Since all H-atoms are negatively charged (gaining electrons), the B-H bonds are polarized. Each B-atom losses 0.591 and 0.626 *e* in forming the B-H_t and B-H_b bonds, respectively, giving rise to a net charge of +1.808.

Table 7: Topological properties of B₂H₆

Name	Bonds	ρ_b (<i>e</i> /Å ³)	$\nabla^2 \rho_b$ (<i>e</i> /Å ⁵)	λ_3 (<i>e</i> /Å ⁵)	BPL (<i>R_b</i> , Å)	GBL (distance) (<i>R_e</i> , Å)
BCP1	B ₁ -H ₂ (b)	0.858	1.123	8.198	1.358	1.312
BCP2	B ₄ -H ₅ (t)	1.274	-9.028	10.724	1.185	1.185
RCPI	-B ₁ - H ₂ - B ₄ - H ₃ -	0.798	-1.682	2.189		

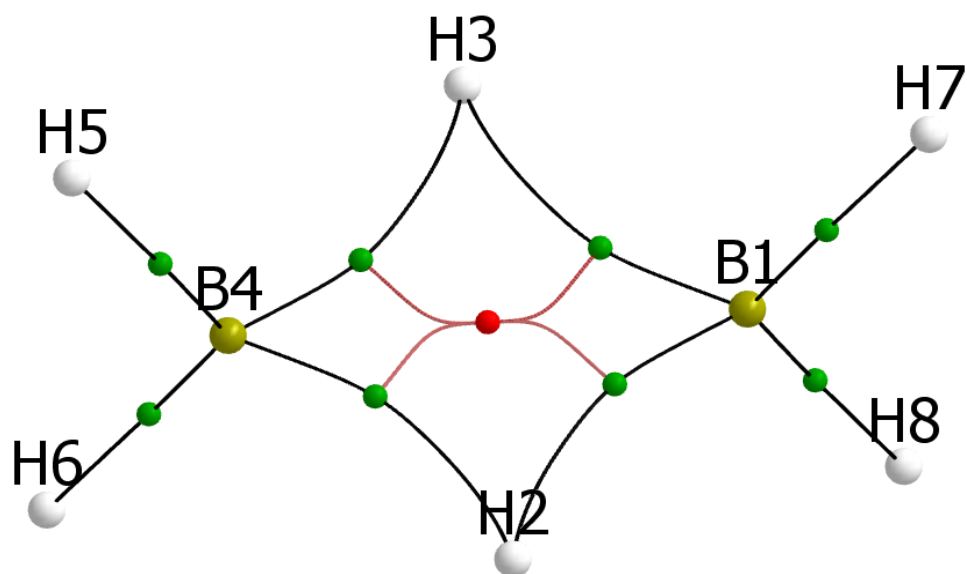


Figure 10: Molecular graphs for B_2H_6 with bond and ring critical points denoted by green and red dots respectively. Note the inwardly curved nature of the bond path linking the bridging protons.

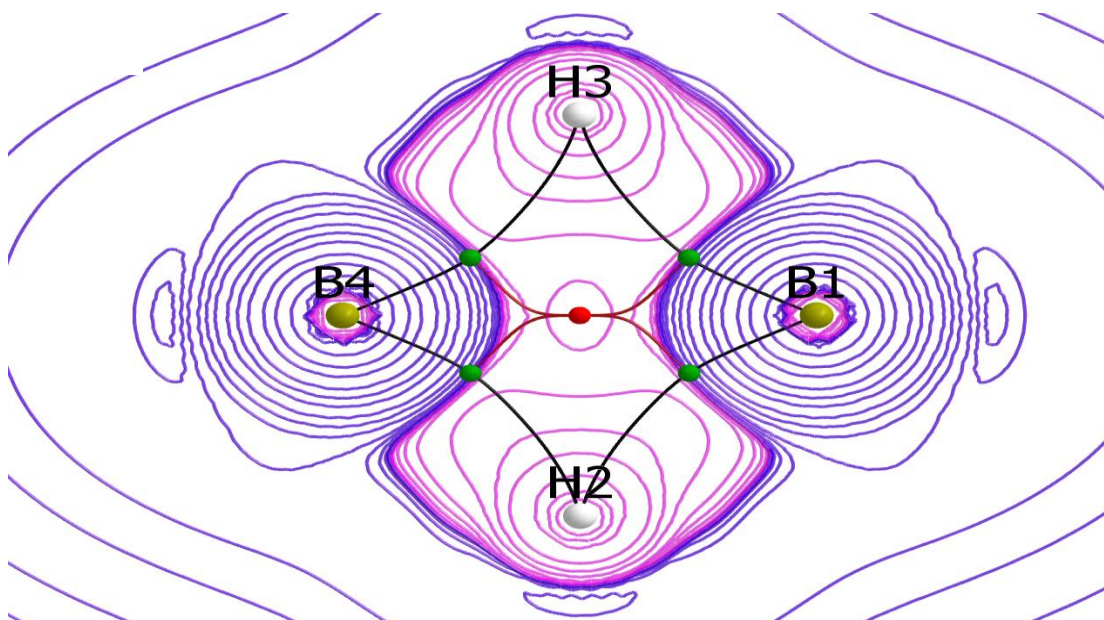


Figure 11: Contour maps of the Laplacian of the electron density for B₂H₆ in the plane of B-H-B Bridge. The pink contour lines depict regions of local charge concentration (negative values) and blue line depict region of local charge depletion (positive value).

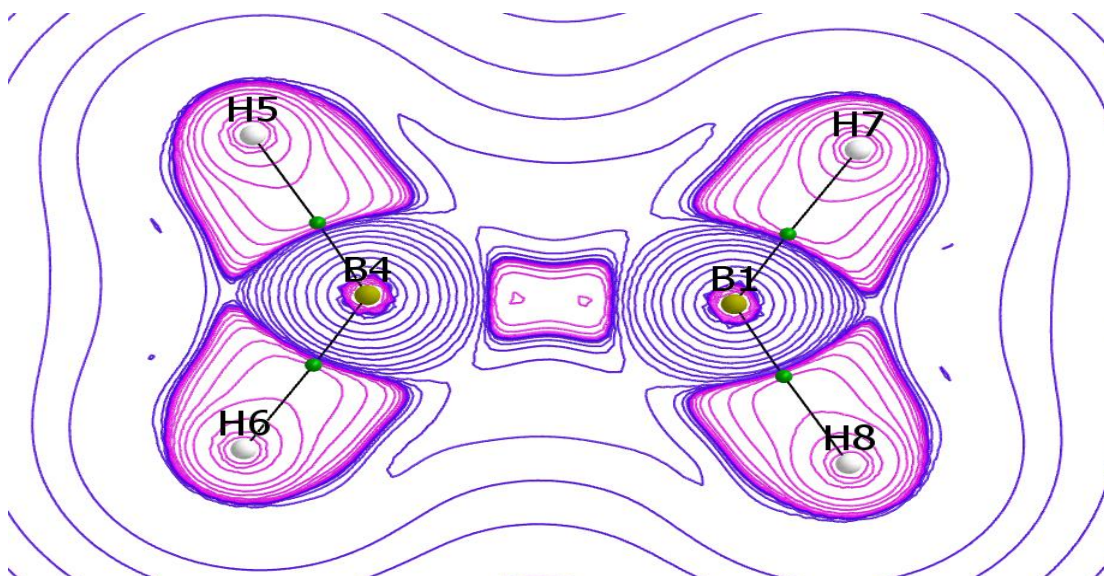


Figure 12: Contour maps of the Laplacian of the electron density ($\nabla^2 \rho_b$) for B₂H₆ in the plane of terminal hydrogen. The pink contour lines depict regions of local charge concentration (negative values) and blue line depict region of local charge depletion (positive value).

Pentaborane, B₅H₉

The result of geometry optimization and atomic coordinates of B₅H₉, adopting the X-ray structure as the initial geometry, is given in Table (A2) (Appendix). The experimental geometry has emerged as a result of combined analysis of X-ray and electron diffraction data, in collaboration and open communication³ of the researchers involved. The C_{4v} molecular symmetry is the consequence of the crystallographic space-group symmetry (Figure 1B) that could be unambiguously determined from the X-ray diffraction pattern recorded by photographic techniques. This information, when used to re-interpret the electron diffraction experiment, turned out to be highly consistent with the data (since gas-phase electron diffraction provides only 1-D structural information, it needs an initial 3D hypothesis). While the two diffraction experiments could be jointly interpreted, the accuracy of the resulting structure does not meet today's standards. The position of the H-atoms, especially those involved in B-H_b-B bridging, has large uncertainty, as manifested by unrealistic mean-square displacement amplitudes. While the H_b positions were accurately obtained with rotational spectroscopy of deuterized species², that study also imposed the C_{4v} molecular symmetry. It is quite surprising that a search in the Cambridge Structural Databank gives only one entry for B₅H₉, which is based on the above discussed film-detected data, meaning that no X-ray diffraction study has been performed on this molecule since 1952. It is even more surprising that this rather inaccurate experimental structure is consistent with a minimum of the BO

energy surface as traced by our calculations at the B3LYP/cc-pVTZ level of theory.

Experimental and Theoretical geometries of B₅H₉

The experimentally³⁴ determined bond distances are compared with the values obtained in this work in Table (8).

Table 8: Comparison of experimental and calculated geometries for B₅H₉

Bonds	Experimental	B3LYP/cc-pVTZ
B _{1ap} - B _{2eq} (apical-equatorial)	1.695 Å	1.690 Å
B _{1eq} - B _{4eq} (equatorial-equatorial)	1.800 Å	1.793 Å
B ₁ - H ₁₀ (terminal)	1.186 Å	1.179 Å
B ₁ - H ₆ (bridging)	1.352 Å	1.343 Å

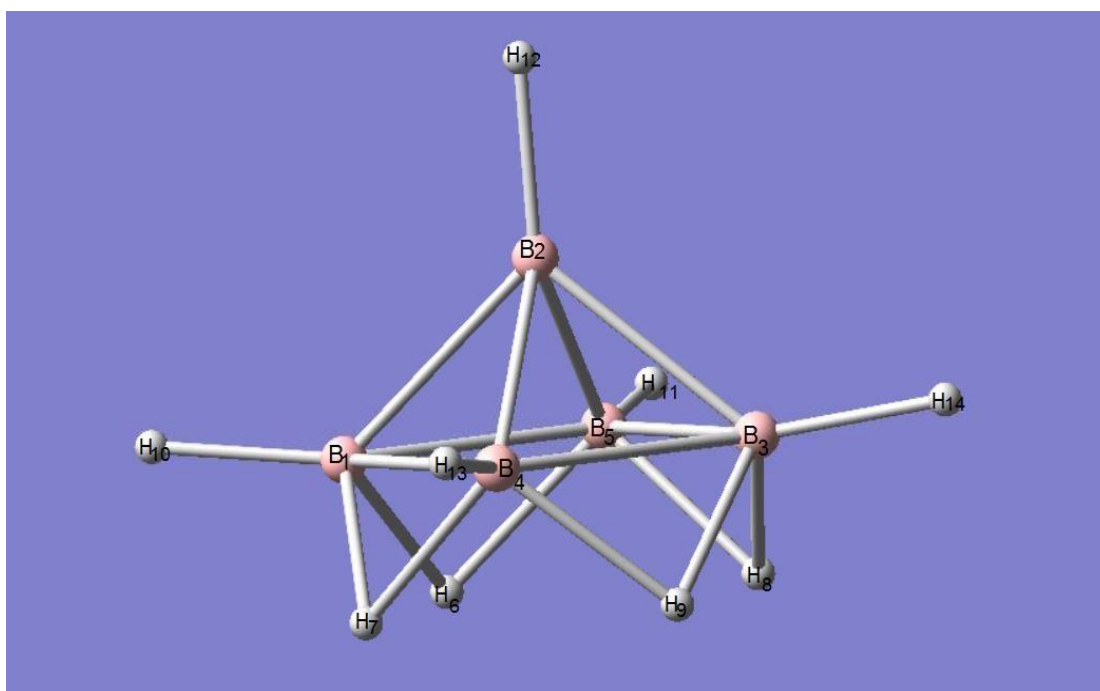


Figure 13: The X-ray structure of B₅H₉

While all but the $B_{ap}-B_{eq}$ experimental bonds are somewhat longer than the optimized ones, the agreements can be considered satisfactory. It is fascinating to note that the equatorial B-B distances are significantly longer than the apical ones implying that the B-B-B rings are not equilateral. This asymmetry immediately raises the question whether the rings are indeed closed, or if the equatorial B-B interactions are to be considered bonds at all (for an internuclear separations of about 1.80\AA). Yet, textbook structural diagrams of pentaborane (9) consistently include the $B_{eq}-B_{eq}$ bond lines (as in Figure 13).

This molecule was a challenge to the localized-MO model for boranes, since the square-pyramidal boron framework with equal $B_{ap}-B_{eq}$ bonds and equivalent B-B bridges is inconsistent with the STYX scheme of (4120). To overcome this issue, the concept of resonance was invoked leading to a combination of four resonance structures (dictated by the symmetry), each containing one closed and one open B-B-B ($3c-2e$) bonding. According to Wade's $(n+2)$ rule¹¹ for nido-boranes, B_5H_9 has 14 skeletal bonding electrons (10 from the five vertices and 4 from the four bridge hydrogens).

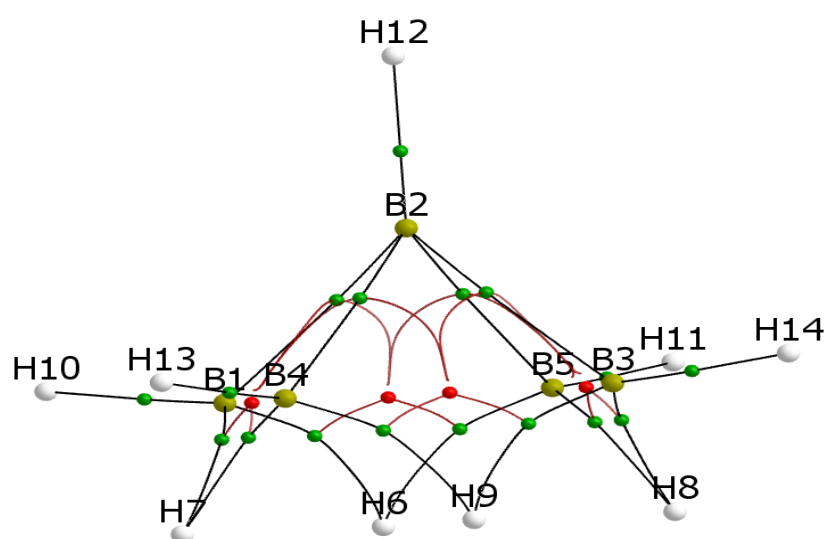
Topological analysis of the electron density of B_5H_9

The topological structure (Figure 14) resembles closely the experimental and optimized molecular geometry (nuclear configuration), the main difference being the lack of direct BP between the equatorial B-atoms. The apical boron atom (B_2) is connected to all basal boron atoms (B_5 , B_3 , B_4 , and B_1) via a straight

BP for each. The BCP indices (Table 9) indicate a weak shared interaction for these bonds. The basal atoms are linked together only with H-bridges whose local topology is similar to that found for diborane; inwardly curved BP and weaker covalent character for B-H_b than for B-H_t bonds. The dominant feature of the topological graph is thus the four equivalent B_{ap}-B_{eq}-H_b-B_{eq} rings, each exhibiting an RCP close in location to the B_{eq}-B_{eq} internuclear axis where a BCPs should be present if these atoms were bonded (as suggested by the resonance model). This situation could formally be viewed as if the two types of CPs were coalesced leading to an unstable structure, which is however not the case, since the RCP has a rank of three. The ring topology is similar to that found for diborane, if one of the bridging H-atom is replaced by a B-atom. The Laplacian plot in the B_{ap}-B_{eq}-H_b-B_{eq} ring's plane in pentaborane (Figure 16) is remarkably similar to the B-H_b-B-H_b ring's plane of diborane (Figure 11). The contour diagram of the Laplacian in the plane of the equatorial boron atoms is shown in Figure 15. There is a continuous region of negative Laplacian along the B_{eq}-B_{eq} interatomic axes indicating local charge concentrations due to the RCPs. Though not associated with electron sharing typical for covalent bonds with BCP, this charge buildup, just like those in the side rings, seems to have a significant contribution to the stability of the molecule and can be taken as a support for the resonance model.

Table 9: Topological properties of B₅H₉

CP	Bond	ρ_b	$\nabla^2 \rho_b$	λ_3	BPL	Distance
BCP1	B ₁ - B ₂	0.937	-4.223	1.024	1.691	1.690
BCP2	B ₁ - H ₆ (b)	0.825	-0.156	5.601	1.397	1.343
BCP3	B ₁ - H ₁₀ (t)	1.275	-8.504	10.837	1.167	1.179
RCPI	-B ₁ - B ₂ - B ₄ - H ₇ -	0.787	-2.086	1.093		

**Figure 14:** Molecular graphs for B₅H₉ with bond and ring critical points denoted by green and red dots respectively.

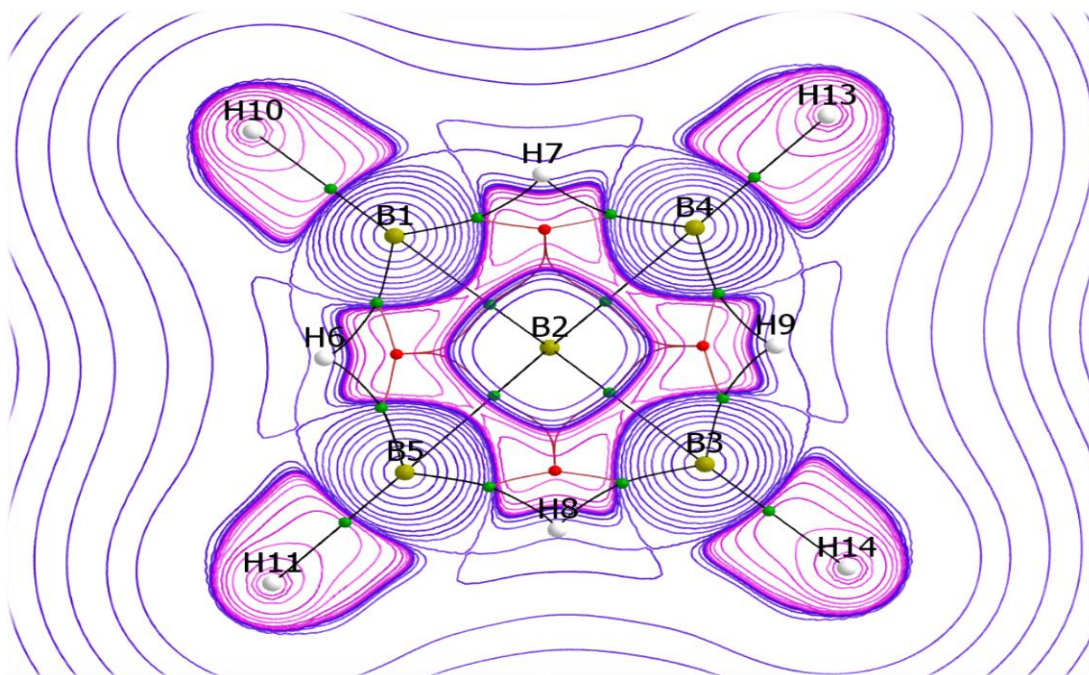


Figure 15: Contour maps of the Laplacian distributions ($V^2 \rho_b$) in the equatorial plane of B_5H_9 . The pink contour lines depict regions of local charge concentration (negative values) and blue line depict region of local charge depletion (positive value).

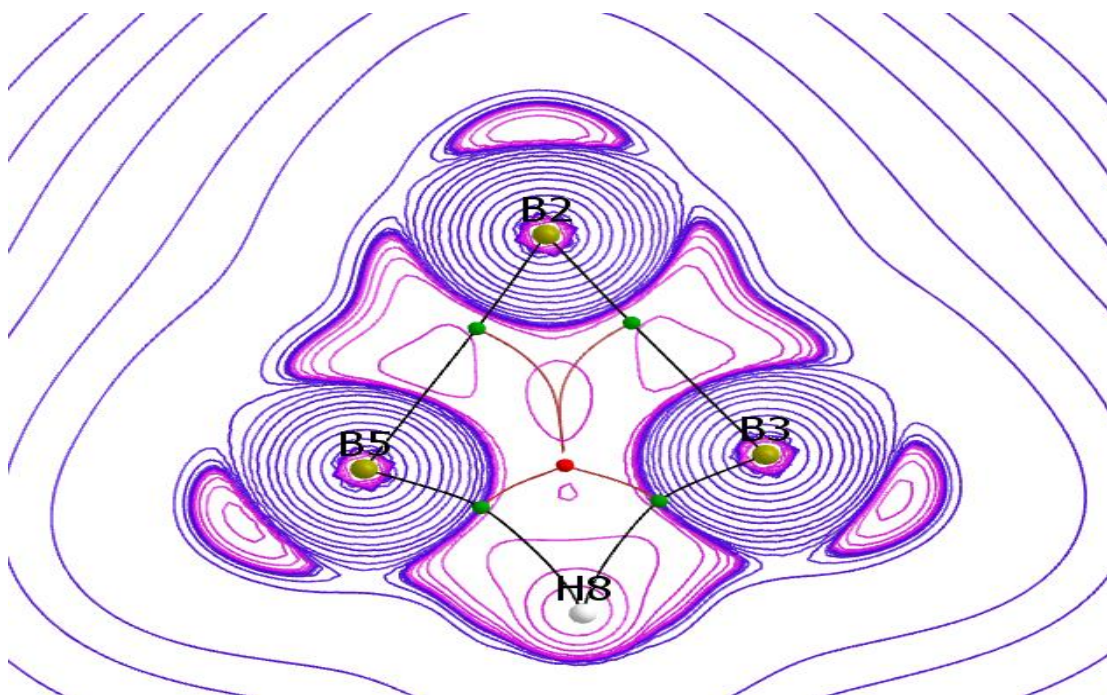


Figure 16: Contour maps of the Laplacian distributions ($V^2 \rho_b$) for B_5H_9 in the plane containing B_2 - B_5 - H_8 - B_3 . The pink contour lines depict regions of local charge concentration (negative values) and blue line depict region of local charge depletion (positive value).

Hexaborane, B_6H_{10}

The energy and optimized atomic coordinates of B_6H_{10} obtained in these calculations are summarized in the Table (A3) (Appendix).

Experimental and Theoretical geometries of B_6H_{10}

Comparison of experimentally³⁴ determined bond distances with those calculated in this work in Table 8 shows a fair agreement.

Table 10: Comparison of experimental^{2, 34} and calculated geometries for B₆H₁₀

Bonds	Experimental (Å)	B3LYP/cc-pVTZ (Å)
B ₁ - B ₂	1.741	1.746
B ₁ -B ₄	1.79	1.796
B ₄ -B ₉	1.741	1.768
B ₂ - B ₄	1.753	1.752
B ₂ - B ₉	1.869	1.811
B ₉ - B ₁₀	1.638	1.634
B ₁ - H ₆ (bridging)	1.321	1.295
B ₄ -H ₆ (bridging)	1.35	1.372
B ₂ - H ₈ (terminal)	1.169	1.181
B ₄ - H ₁₃ (bridging)	1.395	1.323
B ₉ -H ₁₃ (bridging)	1.35	1.332
B ₄ - H ₁₁ (terminal)	1.168	1.179
B ₁ - H ₃ (terminal)	1.141	1.167
B ₉ - H ₁₅ (terminal)	1.171	1.182

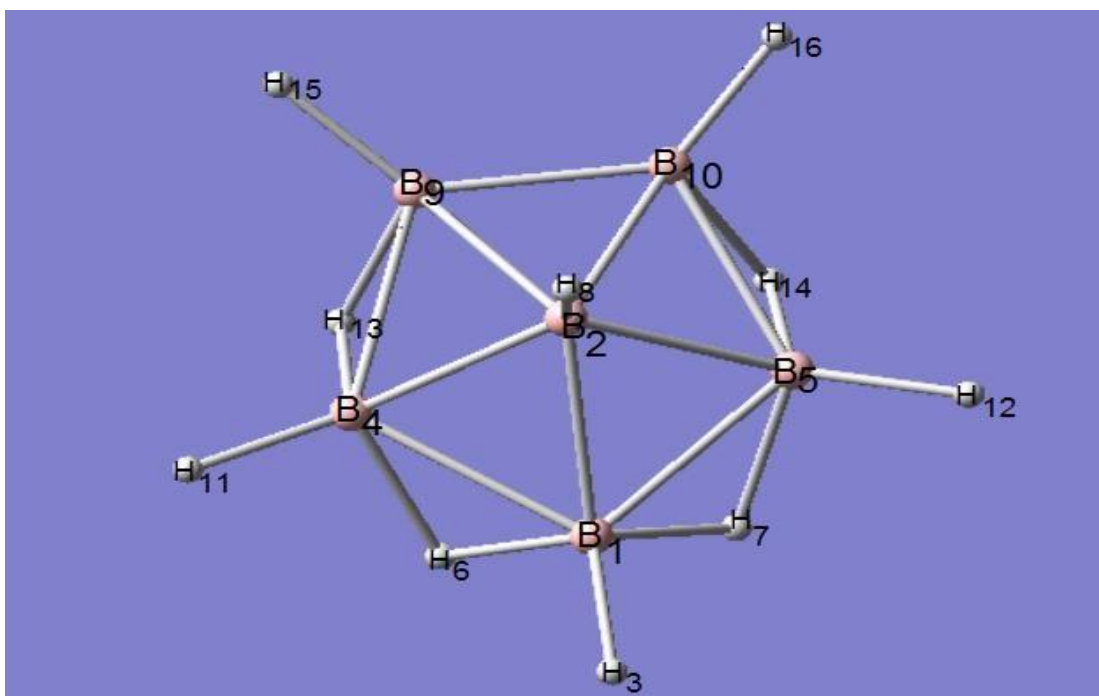


Figure 17: The X-ray and microwave structure of B_6H_{10}

In particular the shortest B_9-B_{10} , as well as the longest B_2-B_9 distance, is accurately reproduced by the theory. However, the calculated B_4-B_9 and B_4-H_6 bonds are significantly longer than the corresponding experimental ones.

According to Wade's rules⁵⁸, B_6H_{10} forms a nido structure with 16 skeletal electrons. The STYX scheme of (4220) restricts the skeletal connectivity to four $B_{eq}-H_b-B_{eq}$ and two $B_{ap}-B_{eq}-B_{eq}$ bridges and one $B_{ap}-B_{eq}$ single bond. The experimental C_s symmetry can be fulfilled by a combination of two resonance forms, each consisting of a closed and an open B-B-B ring, and a B-B bond.

Topological analysis of the electron density of B_6H_{10}

The topological graph (Figure 19) indicates that the equatorial borons are not linked to one another but only to the apical boron B_2 . The only exception is the BP of B_9-B_{10} , each of these atoms being involved only in one H-bridge. Of the $B_{ap}-B_{eq}$ bonds, B_2-B_9 (and its symmetry equivalent B_2-B_{10}) is the weakest link, as it possesses the longest bond path, lowest electron density and negative Laplacian at the BCP. It is also noticeable that these BPs are so bent towards the interior of the ring that their BCPs and RCPs are nearly at the point of coalesce, resulting in two 4-center rings, such as the other two $B_{ap}-B_{eq}-H_b-B_{eq}$ rings (the lower half of the TG in Figure 19). The weakening of these apical interactions (and the opening of the $B_{ap}-B_{eq}-B_{eq}$ rings) seems to correlate with the relative strengthening of the B_9-B_{10} basal interaction which can be considered as a prototype B-B (2c-2e) bond².

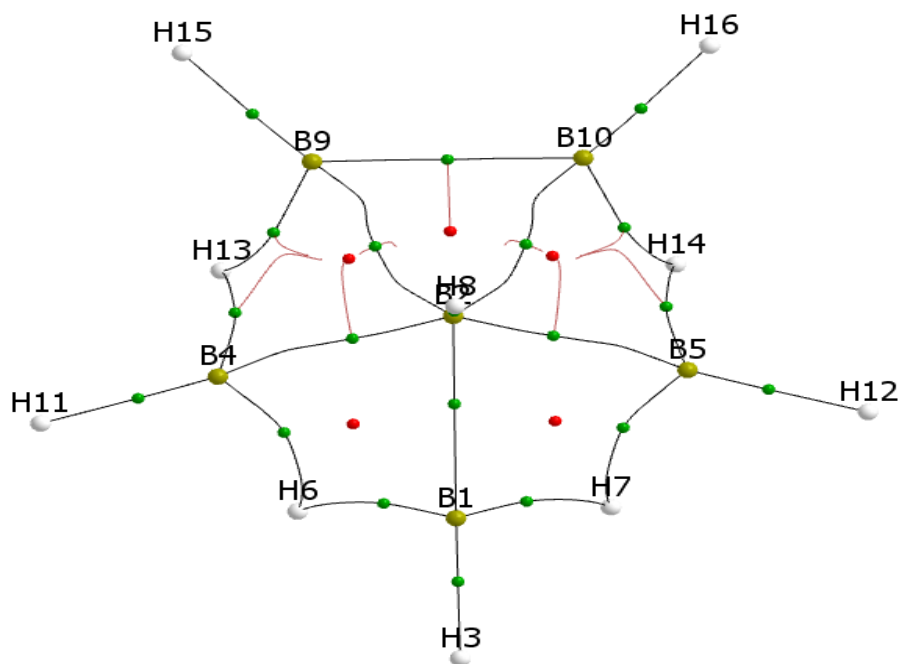


Figure 18: The topological graph for B_6H_{10} with bond and ring critical points denoted by blue and red dots respectively. The trajectories interconnecting the RCPs with the BCP's are not drawn for the lower half of the graph. Note the inwardly curved nature of the bond path linking the bridging protons.

The B-H interactions found in this molecule are topologically equivalent to the corresponding bonds present in diborane and pentaborane (9), except for the basal $B_4-H_{13}-B_9$ bridge which is not symmetric.

The TG exhibits a total of 16 nuclear attractors, 5 RCPs, 20 BCPs and no cage CPs. Thus the Poincare-Hopf relationship is satisfied.

The Laplacian plots for the 3-membered $B_{eq}-B_{ap}-B_{eq}$ side ring (Figure 19) and for the plane of the equatorial borons (Figure 20) exhibit significant charge delocalization due to the presence of RCPs.

Table II: Topological properties B₆H₁₀ (C_s)

CP	Bond	ρ_b	$\nabla^2_{\rho_b}$	λ_3	BPL	Ellipticity
BCP1	$B_1 - B_2$	0.867	-4.468	0.948	1.746	2.054
BCP2	$B_1 - H_3(t)$	1.281	-8.568	10.727	1.167	0.059
BCP3	$B_2 - B_4$	0.858	-4.349	0.994	1.760	2.532
BCP4	$B_1 - H_6(b)$	0.894	0.586	8.619	1.314	1.046
BCP5	$B_2 - H_8(t)$	1.249	-7.121	11.318	1.169	0.013
BCP6	$B_2 - B_9$	0.763	-2.355	1.404	1.869	14.473
BCP7	$B_4 - H_{13}(b)$	0.919	-2.913	4.322	1.395	1.845
BCP8	$B_9 - B_{10}$	1.127	-10.038	0.661	1.638	0.427
BCP9	$B_4 - H_{11}(t)$	1.292	-9.152	10.715	1.1676	0.017
BCP10	$B_9 - H_{15}(t)$	1.255	-7.749	11.168	1.171	0.123
RCPI	$B_2 - B_9 - B_{10}$	0.748	-1.259	1.886		
RCP2	$-B_2 - B_4 - H_{13} - B_9$	0.761	-1.923	1.266		

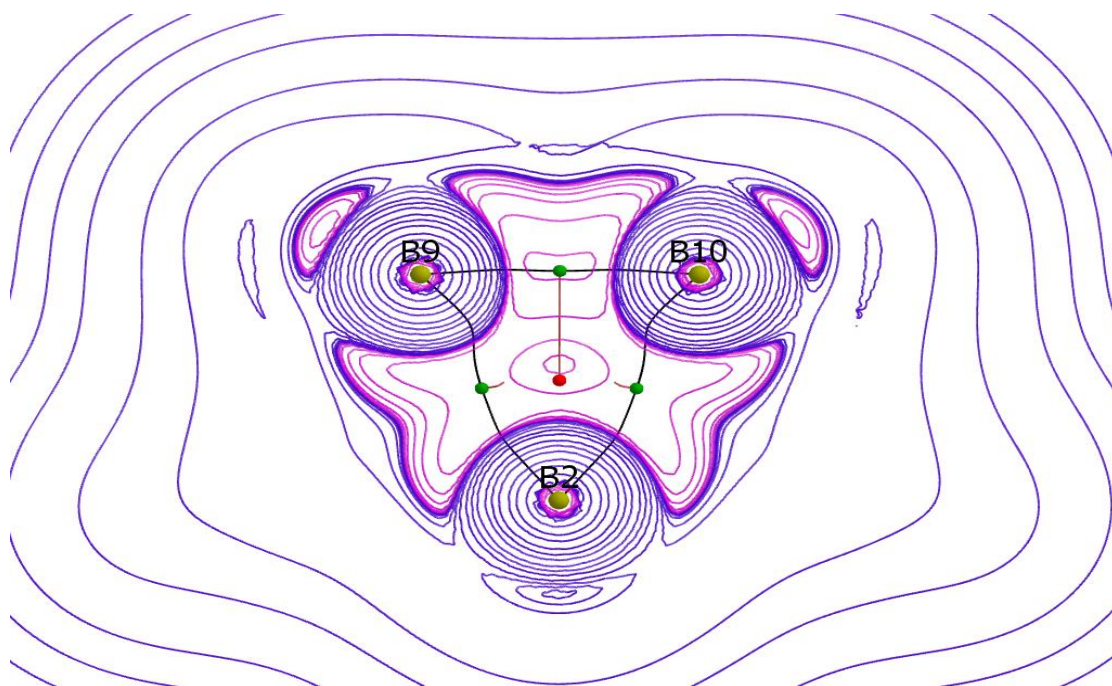


Figure 19: Contour maps of the Laplacian distributions ($V^2 \rho_b$) for B_6H_{10} in the plain containing B_2 - B_{10} - B_9 . It is seen that valence shell charge concentration (VSCC) is higher for B_9 - B_{10} . The pink contour lines depict regions of local charge concentration (negative values) and green line depict region of local charge depletion (positive value)

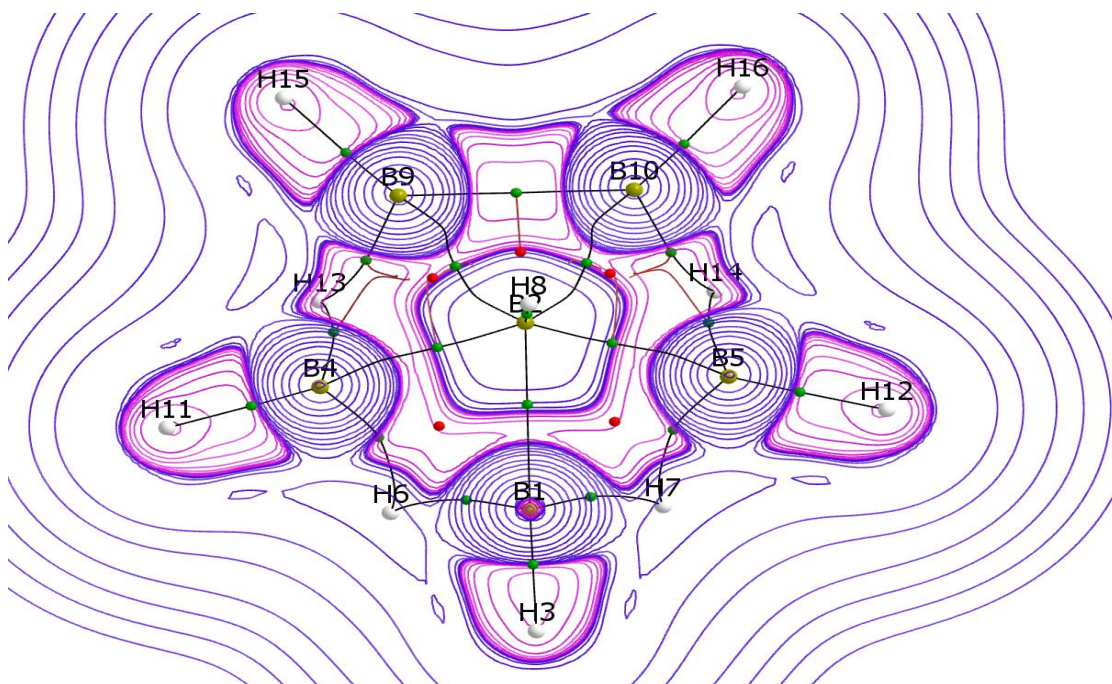


Figure 20: Contour maps of the Laplacian distributions ($V^2 \rho_b$) for B_6H_{10} in plane of equatorial B-B bonds. Notations are the same as in Figure 19

Decaborane, $B_{10}H_{14}$

The energy and optimized nuclear coordinates of $B_{10}H_{14}$ (C_s) obtained in these calculations are summarized in the Table A4 (Appendix).

Experimental and theoretical molecular geometries of $B_{10}H_{14}$

The geometry of $B_{10}H_{14}$ is known from a neutron diffraction study⁵⁹ (Figure 21) and supported by subsequent NMR investigations^{60,61}. The experimentally² determined bond distances are compared with the values calculated in this work in Table 12.

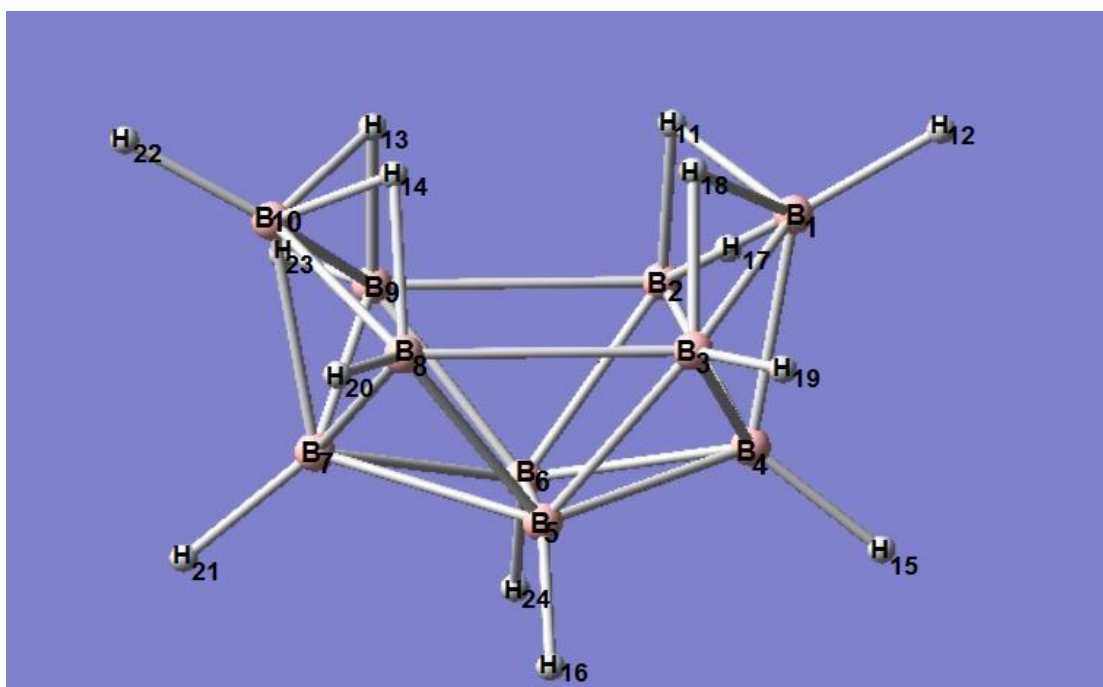


Figure 21: The neutron diffraction structure of $B_{10}H_{14}$

Table 12: Comparison of experimental and optimized geometries for $B_{10}H_{14}$

Bonds or angle	Experimental (Å)	B3LYP/cc-pVTZ (Å)
B_5-B_6	1.71 ³	1.778
$B_6-B_4=B_5-B_7$	1.8 ³	1.78
$B_5-B_4=B_6-B_7$	1.78 ³	1.78
$B_2-B_4=B_7-B_8$	1.76 ³	1.786
$B_3-B_4=B_7-B_9$	1.8 ³	1.786
$B_2-B_1=B_1-B_3=B_9-B_{10}=B_{10}-B_8$	1.77 ³	1.785
$B_1-B_4=B_7-B_{10}$	1.72 ³	1.721
$B_2-B_6=B_5-B_8$	1.78 ³	1.747
$B_3-B_5=B_6-B_9$	1.77 ³	1.747
$B_3-B_8=B_2-B_9$	2.01 ³	2.345
$B_1-H_{11}(\text{bridging})$	1.341 ⁸⁵	1.331

The optimized B_3-B_8 distance (2.345\AA) far exceeds the corresponding experimental value (2.01\AA) indicating that the structure of the isolated (gas-phase) molecule is more open than that in the condensed phase. This is the most significant discrepancy between the structures obtained by the experimental and theoretical methods.

Wade's electron counting rules suggest that 12 ($n+2$, $n=10$) pairs of skeletal electrons are involved in forming 4 ($3c-2e$) $B-H_b-B$, 6 $B-B-B$ and 2 single $B-B$ bonds (STYX:(4620)).

Topological analysis of the electron density of $B_{10}H_{14}$

The 4 $B-H_b-B$ interactions ($B_3-H_{18}-B_1$, $B_1-H_{11}-B_2$ and their symmetry equivalents), as well as the 10 $B-H_t$ bonds exhibit the characteristic topologies (Table 13 and Figure 22) discussed above for the other borane molecules. It appears that these structural units (topological sub-graphs) are fairly well transferable from one molecule to the other. The 6 closed $B-B-B$ bonds, each with an RCP, can also be recovered from the topological structure. As expected, the shortest $B-B$ bond (B_1-B_4 and its equivalent B_7-B_{10}) is apparently more covalent in terms of its bond-topological figures than the others involved in ring formation. It manifest itself as a ($2c-2e$) localized bond, most likely because B_1 (and B_7) does not participate to a $B-H_b-B$ bridge. The Laplacian plots for the two

types of rings (Figure 23 and Figure 24) show the same extended delocalization as found for hexaborane, but with more pronounced charge accumulations.

For this structure we find 24 nuclear attractors, 10 RCPs, 33 BCPs and no cage CP, in accord with the Pointcare-Hopf relationship⁵².

Table B3: Topological properties B₁₀H₁₄ (C_s)

CP	Bond	ρ_b	$\nabla^2_{\rho_b}$	λ_3	BPL	Distan- -ce	Ellipticity
BCP1	B ₁ - B ₄	0.895	-4.921	0.852	1.723	1.721	1.901
BCP2	B ₂ - B ₄	0.812	-3.449	1.262	1.797	1.786	3.808
BCP3	B ₄ - B ₆	0.802	-3.423	1.199	1.786	1.780	3.489
BCP4	B ₃ - B ₅	0.822	-3.912	1.044	1.756	1.747	3.087
BCP5	B ₅ - B ₆	0.805	-3.588	1.277	1.780	1.778	4.094
BCP6	B ₃ - H ₁₈ (b)	0.839	1.326	7.581	1.3621	1.316	1.538
BCP7	B ₁ - H ₁₁ (b)	0.861	-1.065	5.456	1.391	1.331	2.033
BCP8	B ₁ - H ₁₂ (t)	1.290	-9.144	10.580	1.168	1.179	0.023
BCP9	B ₄ - H ₁₅ (t)	1.258	-7.336	11.307	1.168	1.180	0.019

Table 13 (cont.)

CP	Bond	ρ_b	$\nabla^2_{\rho_b}$	λ_3	BPL	Distan- -ce	Ellipticity
BCP10	B ₅ - H ₁₆ (t)	1.260	-7.763	11.014	1.171	1.182	0.031
BCP11	B ₃ - H ₁₉ (t)	1.284	- 8.709	10.800	1.168	1.179	0.022
RCP1	-B ₁ - B ₄ - B ₂ - H ₁₁ -	0.772	-1.650	1.679			
RCP2	-B ₂ - B ₄ - B ₆ -	0.763	-1.419	1.147			
RCP3	-B ₄ - B ₅ - B ₆ -	0.758	-1.479	1.126			
RCP4	-B ₅ - B ₇ - B ₈ -	0.763	-1.419	1.148			

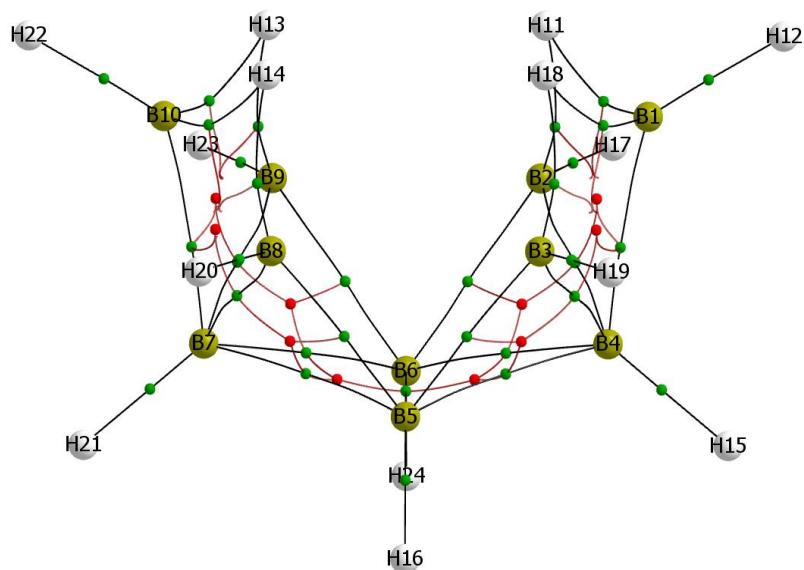


Figure 22: Molecular graphs for $B_{10}H_{14}$ with bond and ring critical points denoted by blue and red dots respectively. Note the inwardly curved nature of the bond path linking the bridging protons.

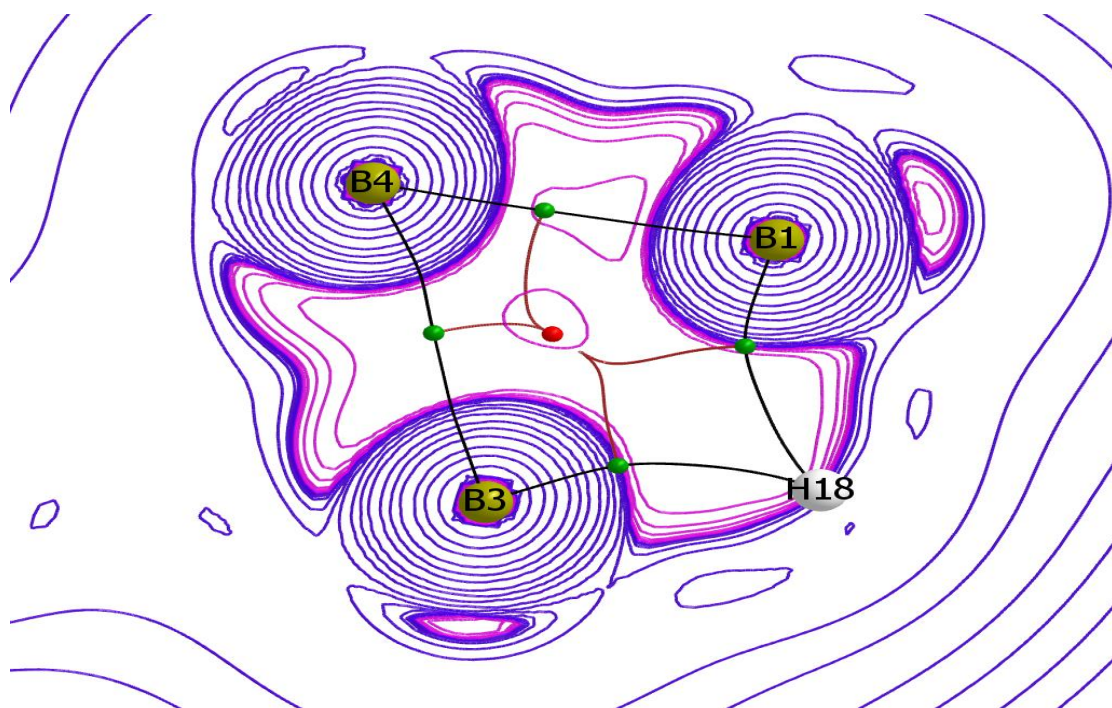


Figure 23: Contour maps of the Laplacian distributions ($V^2 \rho_b$) for $B_{10}H_{14}$ in the plane defined by the B_4 - B_3 - B_1 ring. Pink (blue) contour lines represent negative (positive) values. It is seen that the VSCC is higher for B_1 - B_4 bond

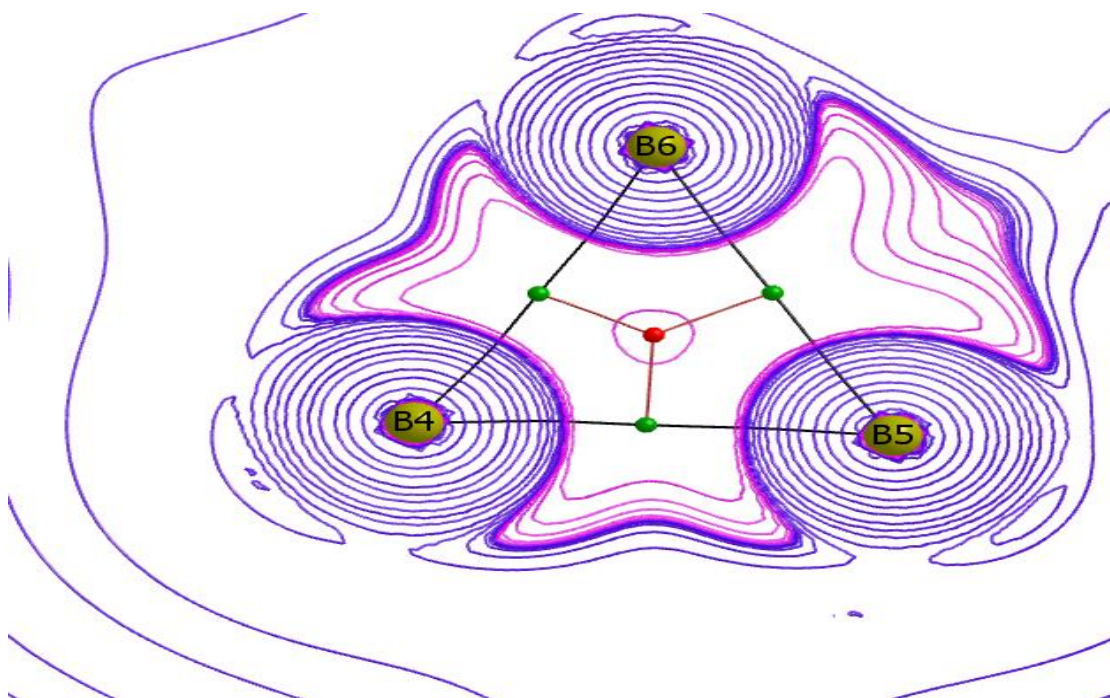


Figure 24: Contour maps of the Laplacian distributions($\nabla^2 \rho_b$) for $B_{10}H_{14}$ in the plane containing B_5 - B_4 - B_6 . The pink contour lines depict regions of local charge concentration (negative values) and blue line depict region of local charge depletion (positive value)

Arachno-Borane, B_4H_{10}

The energy and optimized nuclear coordinates of B_4H_{10} are summarized in the Table (A5) (Appendix).

Experimental and theoretical geometries of B₄H₁₀

Table 14: Comparison of experimental and calculated geometries for B₄H₁₀

Bonds or angle	Experimental	B3LYP/cc-pVTZ
B ₁ - B ₂ (B-B bond)	1.718 Å ⁶⁶	1.716 Å
B ₁ - B ₃	1.854 Å ⁶⁶	1.855 Å
B ₃ - B ₄	2.786 Å	2.816 Å
B ₁ - H ₈ (Bridging)	1.21 Å ⁶²	1.255 Å
B ₄ -H ₈ (Bridging)	1.43 Å ²	1.409 Å
B ₁ - H ₅ (Terminal)	1.19 Å ²	1.180 Å
B ₄ - H ₁₃ (Terminal)	1.19 Å ²	1.190 Å
B ₄ - H ₁₄ (Terminal)	1.19 Å ²	1.185 Å
H ₁₃ -B ₄ -H ₁₄	126° ³⁴	118.845°
B ₁ -B ₂ -H ₆	118°	115.749°
B ₁ -B ₂ -H ₉	109°	111.348°
H ₉ - B ₄ -H ₈	135.7°	137.9°
B ₂ -H ₉ -B ₄	91.1	88.7°

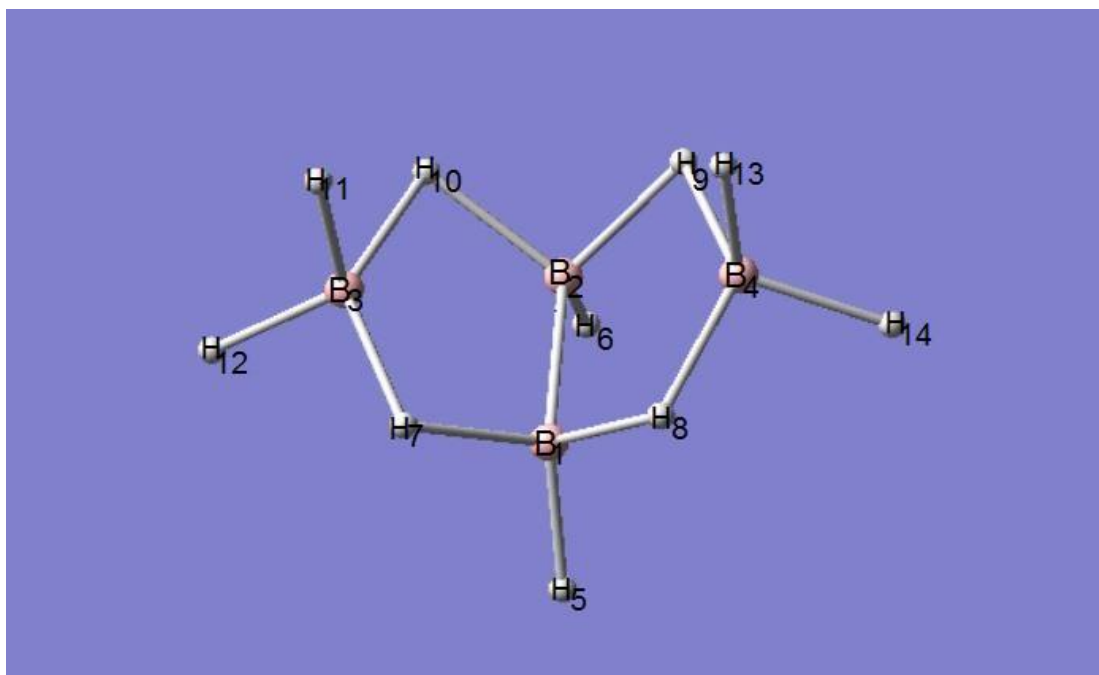


Figure 25: The electron diffraction structure of B_4H_{10} .

It is known from gas-phase electron diffraction experiment⁶⁶ that B_4H_{10} adopts a ‘butterfly’ structure of C_{2v} symmetry (Figure 26). The calculated geometrical parameters of the boron framework are in close agreement with those obtained from the experiment. The B-H_b-B bridges are found to be slightly distorted by both methods. According to the STYX number (4012), the molecule has 4 (3c-2e) B-H_b-B links, one (2c-2e) B-B bond, and 2 BH₂ groups.

Topological analysis of the electron density of B_4H_{10}

The TG (Figure 27) corresponds to the bonding situation predicted by the localized-MO model. The unique B-H_b-B bridge (the other 3 are symmetry

equivalents) is not symmetric; one of the B-H_b BP is longer than the other and the BCPs are slightly shifted toward the B-atom, implying non-local polarization. Two such bridges (on each side of the ‘butterfly’) form a 5-membered (non-planar) B-H_b-B-H_b-B ring, two of which are fused together at the B-B central bond situated in the mirror plane. The BPs are inwardly curved that is characteristic of electron delocalization seen also on the Laplacian map depicted in Figure 27.

Table 15: Topological properties B₄H₁₀ (C_{2v})

CP	Bond	ρ_b	$\nabla^2_{\rho_b}$	λ_3	BPL	Distance
BCP #						
1	B ₁ - B ₂ (B-B)	0.938	-6.650	0.877	1.719	1.716
2	B ₄ - H ₈ (b)	0.719	0.512	3.995	1.500	1.409
3	B ₁ - H ₅ (t)	1.260	-7.514	11.035	1.168	1.180
4	B ₁ - H ₈ (b)	0.951	-0.815	10.973	1.255	1.255
5	B ₄ - H ₁₃ (t)	1.252	-8.493	10.383	1.179	1.190
6	B ₄ - H ₁₄ (t)	1.274	-8.947	10.648	1.174	1.185
RCP #						
1	-B ₁ - B ₂ - H ₁₀ - B ₃ - H ₇ --	0.644	-0.9405	1.485		

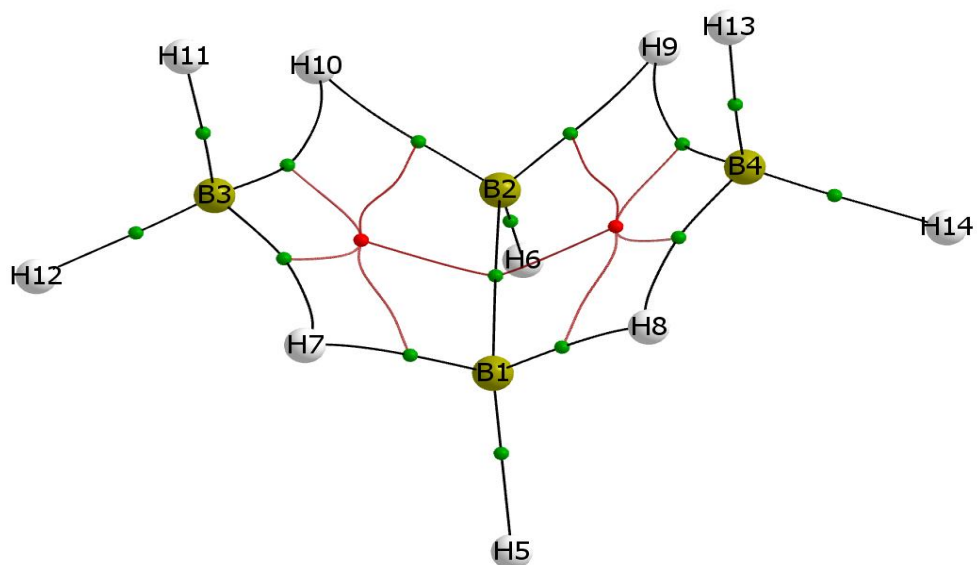


Figure 26: Molecular graphs for B_4H_{10} with bond and ring critical points denoted by blue and red dots respectively. Note the inwardly curved nature of the bond path linking the bridging protons.

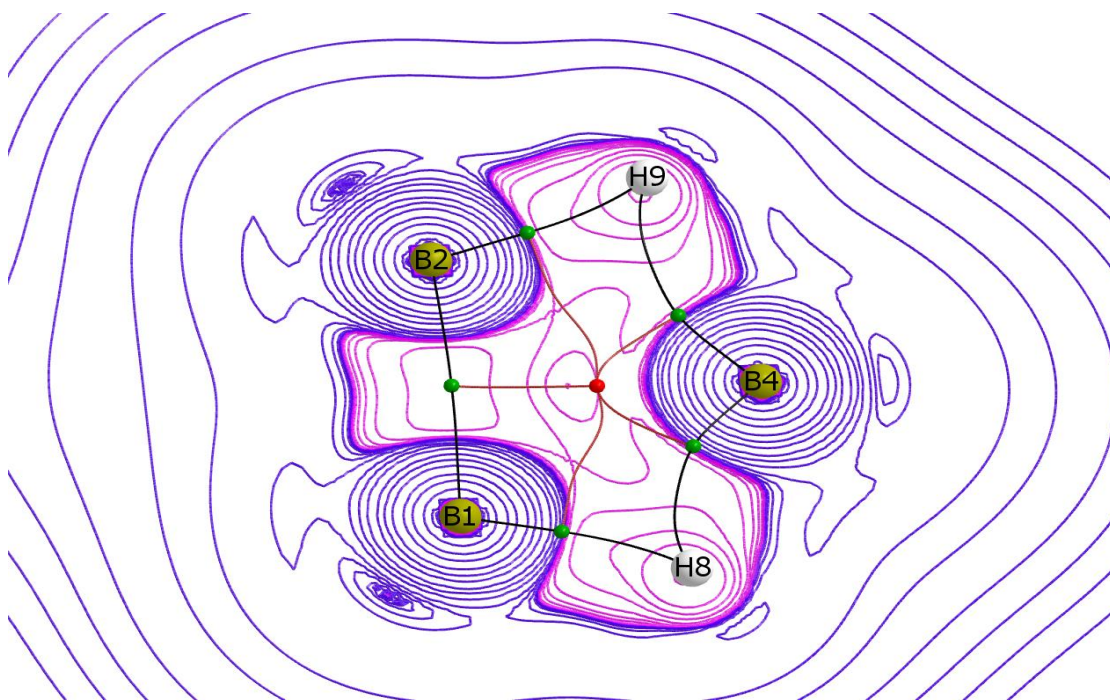


Figure 27: Contour maps of the Laplacian distributions ($V^2 \rho_b$) for B_4H_{10} in the plane containing B_1 - H_8 - B_4 - H_9 - B_2 . The pink contour lines depict regions of local charge concentration (negative values) and blue line depict region of local charge depletion (positive value). It is seen that the VSCC is higher for B_1 - H_8 bond than that for B_4 - H_8 .

Closo-Borane, $B_6H_6^{2-}$

The energy and optimized nuclear positions of $B_6H_6^{2-}$ are listed in the Table (A6) (Appendix).

Experimental and theoretical geometries of $B_6H_6^{2-}$

The structure was determined by electron diffraction³⁴ (Figure 28). We started the geometry optimization with nuclear coordinates obtained at the HF level³⁴. The B3LYP gives significantly lower electronic energy and a slightly different

geometry (Table A7). Comparison of optimized and experimental data (Table 16) reveals the former bonds to be significantly longer than the latter ones.

Table 16: Comparison of experimental and calculated bond distances for $B_6H_6^{2-}$

Bonds or angle	Experimental (Å)	B3LYP/cc-pVTZ (Å)
$B_1 - B_2$	1.69 ⁴⁹	1.732
B_2-B_4		2.45
$B_6 - H_7$	1.11 ⁴⁹	1.212

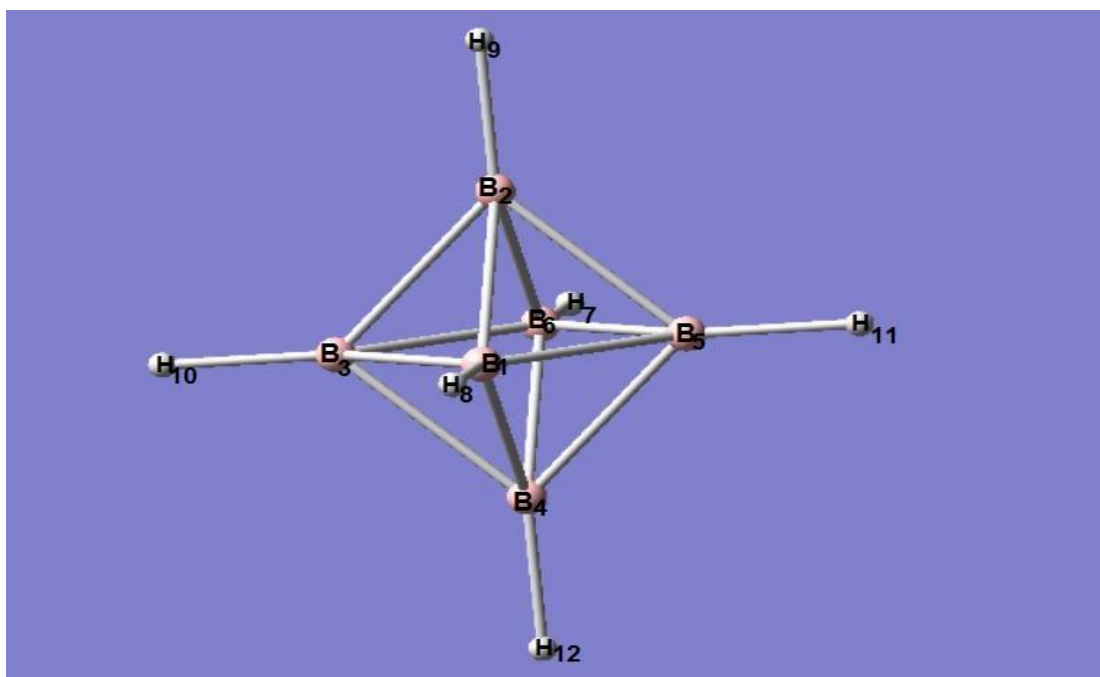


Figure 28: The electron diffraction structure of $B_6H_6^{2-}$.

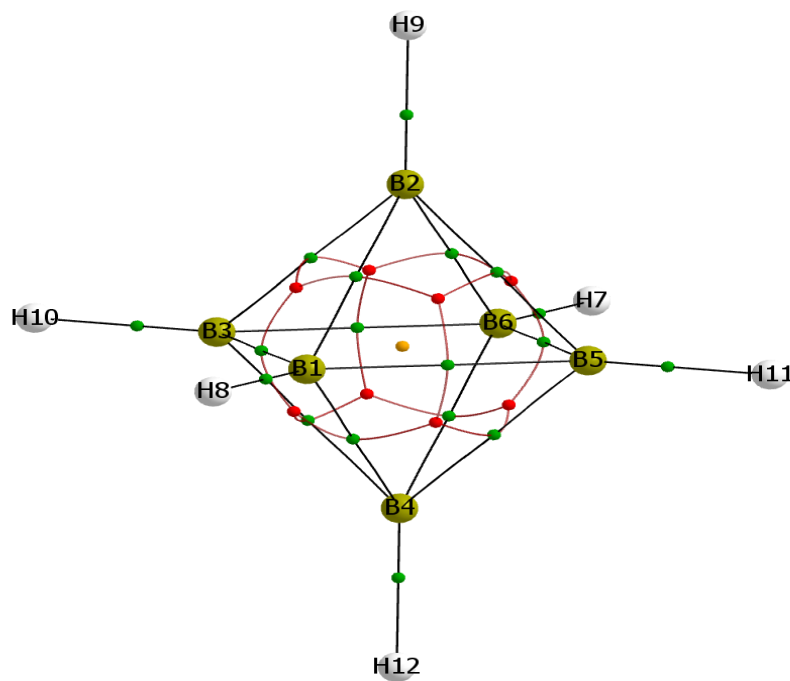
Closo-boranes form cage structures with B-B bonds defining an n -vertex polyhedron (n B-atoms, each bonded to one H-atom) marked by the STYX number (0, n -2,3,0). The O_h symmetry of $B_6H_6^{2-}$ is the consequence of the extra two electrons.

Topological analysis of the electron density of $B_6H_6^{2-}$

The TG of the boron framework (Table 17 and Figure 29) is a perfect hexagon described by 5-coordinated B-vertices and equilateral 3-membered B-rings fused at the B-B edges. The symmetry independent unit can thus be considered as the prototype of closed B-B-B interactions without H-bridging. The B-B BPs are straight (BPL=distance) and exhibit a topology similar to that of the B-H_t bonds (at the borderline of shared and closed-shell interactions). Further details are revealed by the Laplacian distribution for a 3-membered B-ring (Figure 30) which shows a pronounced charge delocalization of three-fold symmetry in the bonding region of B-B interactions.

Table 17: Topological properties of $B_6H_6^{2-}$ (Symmetry O_h)

CP	Bond	ρ_b	$\nabla^2 \rho_b$	λ_3	BPL	Distance
BCP1	B ₁ - B ₂	0.857	-3.618	1.138	1.733	1.732
BCP2	B ₆ - H ₇ (t)	1.075	-3.175	11.752	1.202	1.212
RCPI	-B ₄ - B ₅ - B ₆ -	0.796	-0.912	1.266		
CCPI	-B ₁ - B ₂ - B ₃ - B ₄ - B ₅ - B ₆ -	0.434	6.509	2.169		

**Figure 29:** Molecular graphs for $B_6H_6^{2-}$ with bond, ring and cage critical points denoted by green, red and orange dots respectively.

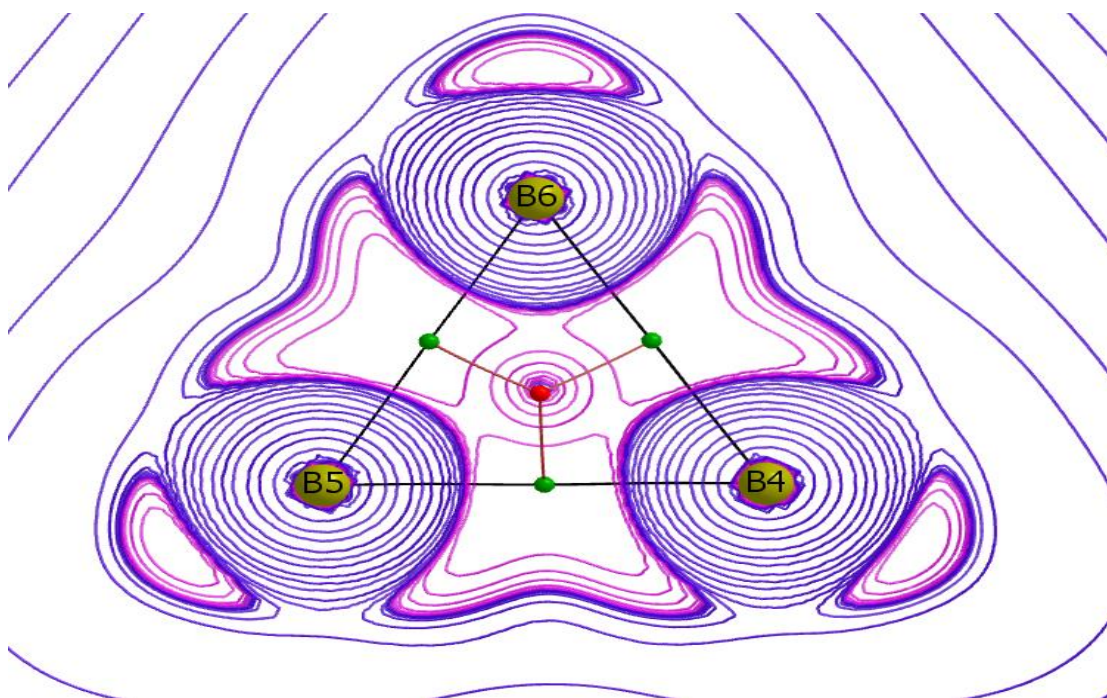


Figure 30: Contour maps of the Laplacian distributions ($\nabla^2 \rho_b$) for $B_6H_6^{2-}$ in the plane containing B_4 - B_5 - B_6 . The pink contour lines depict regions of local charge concentration (negative values) and blue line depict region of local charge depletion (positive value).

The Dynamic Electron Density of Boranes

The QTAIM states that a molecular graph is the collection of bond paths. A BP is formed by two special trajectories of $\nabla \rho$; both originate at the BCP (a (3,-1) CP) and each terminates at different nuclei ((3,-3) CPs), defining in this way, an interaction line between the interacting nuclei. Since the ED is maximum along the BP relative to any other path interconnecting the nuclei, this trajectory is considered to be a geometrical representation of electronic forces balancing

nuclear repulsion and has been shown to be a necessary and sufficient condition for a bond formation between two atoms in a stationary molecule ($\rho(\mathbf{r}, \mathbf{R}^0)$)²⁵. If the molecular graph, defined in such a way, is preserved for nuclear arrangements in the close neighborhood of a minimum of the BO hypersurface (the stationary geometry, \mathbf{R}^0), it represents a stable structure. More specifically, every CP of a stable graph must have rank three (3 no-zero curvatures) and must be linked to other CP(s). Furthermore, the number of CPs (N) of each type must satisfy the Poincare-Hopf relationship.

The nuclear arrangements in question naturally include those which are accessible via small displacements from the equilibrium geometry due to harmonic vibrations. Thus the vibrating molecule on average should be topologically equivalent to the stationary molecule, that is, the dynamic ED (a Boltzmann average over all vibrational modes) must have the same number and types of CPs as the stationary ED calculated at the equilibrium nuclear configuration.

The ‘exact’ dynamic ED cannot be evaluated in a closed analytic form. The convolution approximation²² introduced for modeling X-ray diffraction data provides an analytically tractable route to thermal smearing, since it relates the dynamic ED with the stationary one. In other words, the density units (products of basis functions) comprising the total static ED, are assumed to rigidly follow the motion of the nucleus (or nuclei) they are centered at (or between). To

elucidate the effect of internal vibration modes on the bonding situation of boranes, we evaluated the topology of the convolutional dynamic ED ($T=300\text{K}$) for each of the molecule examined in this study.

For the calculations, that require the harmonic internal normal modes and the corresponding frequencies obtained for the equilibrium structures, we utilized a new version of the Denprop program. The convolution functionality was implemented by R. Michael, a Ph.D. graduate from our group.

The comparison of static and dynamic EDs reveals their topologically equivalence for all molecules. As for the bond topological figures and the Laplacian, there are differences to comment on. We find that the CPs of the static ED are only slightly affected by thermal smearing, but with a characteristic trend; $\langle \rho_{BCP} \rangle_T < \rho_{BCP}$ and $\langle \nabla^2 \rho_{BCP} \rangle_T < \nabla^2 \rho_{BCP}$ for all bonds. This observation is summarized in Table 18 for representative bonds in the boranes we studied. The changes in the Laplacian (and the principal curvatures) due to nuclear vibrations are however significant and have chemical relevance. These effects are portrayed on Figure 31, Figure 32 and Figure 33 in terms of difference curvatures ($\langle \lambda_j \rangle_T - \lambda_j; j = 1,2,3$) obtained by tracing the relevant bonds and the $\text{H}_b\text{-H}_b$ internuclear line in diborane. The bond profile of the Laplacian appears to be dominated by the bond-parallel curvature (λ_3), since λ_1 and λ_2 contributes almost identically (only one of them is drawn on Figure 31, Figure 32 and Figure 33) and to a lesser extent. The maps of the difference Laplacian ($\langle \nabla^2 \rho \rangle_T - \nabla^2 \rho$) in the two mirror

planes of diborane defined by the B-H_b-B bridge (Figure 31) show the changes in 2D corresponding to those discussed above in 1D for the B-H_b bond. The prominent features displayed by this map is the effective charge migrations from the atomic toward the VSCC regions.

Table 18: Topological Properties at of Static and Dynamic EDs. Comparison of ρ ($e/\text{\AA}^3$;), $\nabla^2\rho$ ($e/\text{\AA}^5$;) and λ_i ($e/\text{\AA}^5$;) in Boranes

Bond (molecules)		Static	Dynamic
B-B (B ₄ H ₁₀)	ρ	0.938	0.933
	$\nabla^2\rho$	-6.650	-6.580
	λ_3	0.877	0.783
B-B (B-B-B) (B ₆ H ₆ ²⁻)	ρ	0.857	0.853
	$\nabla^2\rho$	-3618	-3.614
	λ_3	1.138	1.049
B-H _t (B ₂ H ₆)	ρ	1.274	1.249
	$\nabla^2\rho$	-9.028	-8.085
	λ_3	10.724	8.131
B-H _b (B ₂ H ₆)	ρ	0.858	0.856
	$\nabla^2\rho$	1.123	0.782
	λ_3	8.198	7.610
RCP (B ₂ H ₆)	ρ	0.798	0.799
	$\nabla^2\rho$	-1.682	-1.589
	λ_3	2.189	2.046
CCP (B ₆ H ₆ ²⁻)	ρ	0.434	0.432
	$\nabla^2\rho$	6.509	6.472
	λ_3	2.169	2.157

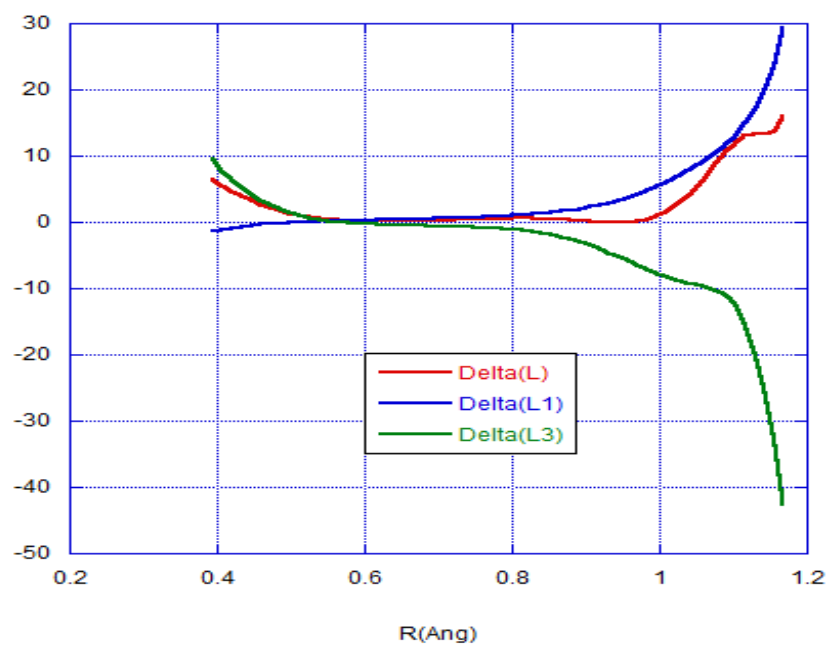


Figure 3l: Change in the curvatures caused by thermal smearing calculated for the B_1-H_2 bond path in B_2H_6 . Each curve represents differences between dynamic and static properties as a function of distance from the B-atom: $(V^2\rho)_T - V^2\rho$ (Delta(L)), $(\lambda_1)_T - \lambda_1$ (Delta(L1)) and $(\lambda_3)_T - \lambda_3$ (Delta(L3)).

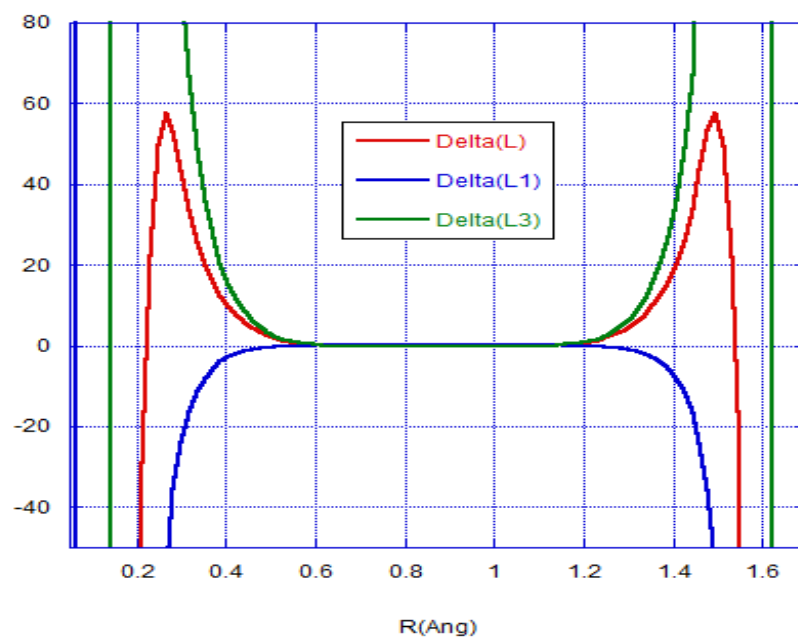


Figure 32: Change in the curvatures caused by thermal smearing calculated along the axis of the bridging H-atoms ($H_2...H_3$) in B_2H_6 . Notations are the same as in Figure 31.

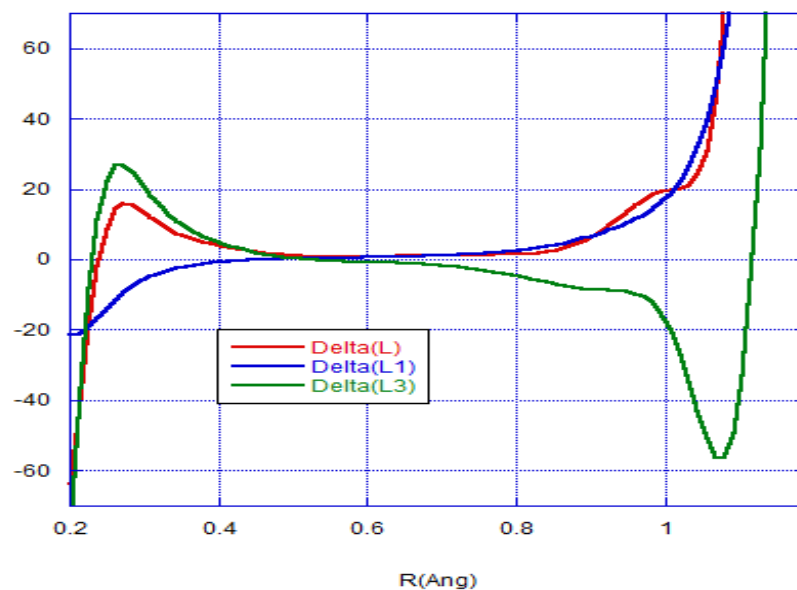


Figure 33: Change in the curvatures caused by thermal smearing calculated along the terminal B₁-H₇ bond in B₂H₆. Notations are the same as in Figure 31.

The overall effect of thermal smearing on the Laplacian distribution can be visualized by plotting the dynamic function with reference to the static one: $\langle \nabla^2 \rho \rangle_T - \nabla^2 \rho$. Such a difference contour map is displayed in Figure 35 for the bridging plane of diborane, explicitly showing how the regions of charge accumulation and depletion change upon nuclear vibrations.

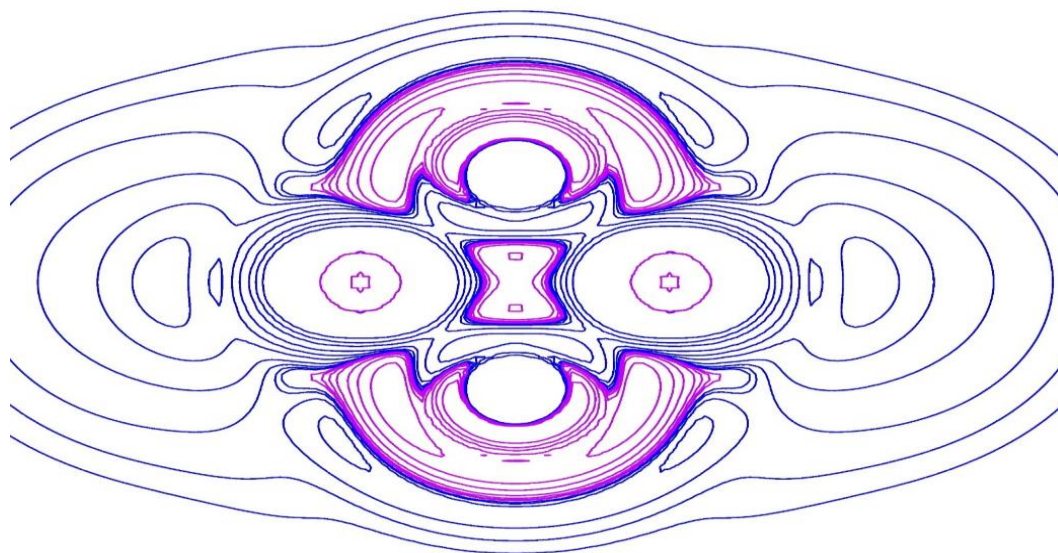


Figure 34: Contour map of change in the Laplacian distribution caused by thermal smearing calculated for the B-H_b-B bond path in B₂H₆.

5 CONCLUSION

In this work we invoked the QTAIM to study the bonding situations in boranes for which the classical Lewis model fails and the localized-MO (or valence-bond) description needs to be extended. The ED of representative borane molecules are calculated in terms of KS molecular orbitals at the B3LYP/cc-pVTZ level.

For the interaction between a given pair of atoms in a molecule, the value of ρ_{BCP} usually directly related to the strength (bond-order) of the interaction. This correlation, in conjunction with other bond-topological descriptors, can be used to establish a pattern for the relative strength (covalent / ionic character) of chemically equivalent or similar bonds. In accord with the results of earlier computational studies [Bade & Leagare], we find three types of characteristic interactions for the molecules considered; the (2c-2e) bonds (B-Ht and single B-B bonds) and the weaker (3c-2e) bonds (using the traditional localized-MO terminology).

The former interactions appear to be of localized, shared type ($\nabla^2 \rho_{BCP} < 0$ and ρ_{BCP} is relatively large in value, indicating contraction of the ED towards the BP). The lack of continuous charge concentration interconnecting the atomic basins is reflective of a strong polar character (ionic) of the B-Ht bonds (which is reflected also in the integrated charges). These interactions seem to be unique and highly transferable from one molecule to the other, that is, their topological figures exhibit the least variation through the series of molecules studied in this

work. The single B-B bond, found in boranes, is also an intermediate between shared and closed-shell interactions; topologically similar to the B-H_b bond, but exhibits joined valence shell charge concentrations. The B_{eq}-B_{ap} (basal-apical) bonds in B₅H₉ and B₆H₁₀ are markedly weaker than the single B-B bond in B₄H₁₀.

Relative to these bonds, the B-H_b links in nido- and arachno-boranes can be characterized as closed-shell interactions ($\nabla^2 \rho_{BCP} \leq 0$ and ρ_{BCP} is low in value). They also show lower degree of transferability than the B-H_t interactions (for example, in B₄H₁₀ they are not equivalent).

Most importantly, the (3c-2e) linkages are not localized but fused to form 3-, 4- and 5- membered rings. Unlike in the carbon analogs, the ring bonds in boranes have inwardly curved BPs (a characteristic feature of these bonds). At the RCP (3,+1) the density is minimum in the plane defined by the two eigenvectors corresponding to the positive principal curvatures (eigenvalues) and maximum along the third eigenvector normal to the ring's plane. The maximum of the density in this direction however exceeds in value those found at the BCP of the bonds forming the rings in boranes. The topology at the RCP is dominated by the negative curvature; $\nabla^2 \rho_{RCP} = \lambda_1 + \lambda_2 + \lambda_3 < 0$, to such an extent that $\nabla^2 \rho_{RCP} < \nabla^2 \rho_{BCP}$ for all peripheral B-H_b linkages. Since the RCP is located at, or close to, the internuclear B-B axis (in nido- and arachno-boranes), the charge accumulation due to the RCP virtually resembles that of a BCP. According to the local virial relationship, if the density is relatively high and its Lapcian is negative,

the potential energy density has a stabilizing role (it locally dominates over the kinetic energy and thus lowers to total energy). Hence, the charge accumulations over the rings' surfaces, implying multicenter electron delocalization (often termed as 3D aromaticity), can indeed have a significant contribution to the stability of these systems. In other word, rings rather than localized (3c-2e) bonds are the main topological building blocks of borane structures.

A novel component of this thesis is the extension of the topological analysis to the dynamic ED. The most important finding is that the dynamic and stationary EDs are topologically equivalent (including the terminal B-H bonds), within the convolution approximation (assuming no electronic-state crossing each and / or excitation occurs during nuclear vibrations). This means that the T-dependent TGs remain invariant even at 300K for these light-atom molecules, suggesting that they indeed correspond to stable structures. While the BCP indices remain mostly unaltered, the VSCCs (local maxima of $-\nabla^2\rho$) undergo significant changes upon vibrational smearing of the ED.

As an important conclusion we emphasize the potential interpretive power of topological analysis of $\langle\rho\rangle_T$, since it is a 'thermodynamic property' (refers to a molecule in thermal equilibrium with its surrounding and thus T-dependent) and encompasses the molecular structure concept (the equivalent class of topological graphs) as emerged from the QTAIM. Such analyses can open new revenues for studying reactive properties of molecules, since nucleophilic or

electrophilic sites identified by the topology of the Laplacian can be markedly affected by vibrations.

REFERENCES

1. R.M. ADAMS, Nomenclature of inorganic boron compounds, *Pure Appl, Chem*, 30, 683-710 (1972).
2. William N. Lipscomb, *Boron Hydrides*, W.A. Benjamin , Inc., New York, 1963.
3. W. Dilthey, *Z . Angew. Chem.*, 34, 596 (1921). Uber die Konstitution des Wassers.
4. C. E. nordman and W.N. Lipscomb, *J. Am . Chem . SOc.*, 75, 4116(1953).
The molecular structure of B₄H₁₀.
5. C. E. nordman and W.N. Lipscomb, *J. Am . Chem.phys.*, 21,1856 (1953).
The crystal and molecular structure of tetraborane.
6. W.J. Dulmage and W. N. Lipscomb, *J . Am. Chem . Soc.*, 73, 3539 (1951).
The molecular structure of pentaborane .
7. W.J. Dulmage and W. N. Lipscomb, *Acta Cryst.*, 5,260 (1952). The crystal and molecular structure of pentaborane.
8. L. pouling and S. Weinbaum, *Z.Krist.*, 87, 181 (1934). The structure of calcium boride.
9. J.S. kasper, C. M. Lucht, and D. Harker, *Act Cryst.*, 3, 436 (1950). The crystal structure of decaborane ,B₁₀H₁₄. A primary report of the boron positions by these authors is published in the *J Am Chem Soc.*, 70 881(1948). In the present paper Interatomic distances have been recalculated from the final parameters of the 1950 paper.

10. W.H. Eberhardt, B.L. Crawford, Jr., and W.N. Lipscomb, *J Chem. Phys.*, 22, 989(1954). The valence structure of boron hydrides
11. K. Wadw, *Adv. Inorg. Chem. Radiochem.*, 1976, 18, 1.
12. J. Robert Michael, *Analysis of Thermal Motion Effects on the Electron Density via Computational Simulation.*, Middle Tennessee State University December, 2014.
13. Ian de Joncheere Kirke, *Computational Study of Covalency and Complexation in Actinides using Static and Dynamic Simulation and Topological Density Analysis*, University College London, June21,2013.
14. P. Hohenberg and W. Kohn. Inhomogeneous electron gas. *Phys. Rev.* 136:B864–B871, 1964.
15. W. Kohn and L. J. Sham. Self-consistent equations including exchange and correlation effects. *Phys. Rev.* 140 : A1133- A1138, 1965.
16. K. Kim; K. D. Jordan (1994). "Comparison of Density Functional and MP2 Calculations on the Water Monomer and Dimer". *J. Phys. Chem.* **98** (40): 10089–10094. [doi:10.1021/jl00091a024](https://doi.org/10.1021/jl00091a024)
17. P.J. Stephens; F. J. Devlin; C. F. Chabalowski; M. J. Frisch (1994). "*Ab Initio* Calculation of Vibrational Absorption and Circular Dichroism Spectra Using Density Functional Force Fields". *J. Phys. Chem.* **98**(45): 11623–11627.
18. A. D. Becke (1988). "Density-functional exchange-energy approximation with correct asymptotic behavior". *Phys. Rev. A* **38**(6): 3098–3100.

19. Chengteh Lee; Weitao Yang; Robert G. Parr (1988). "Development of the Colle-Salvetti correlation-energy formula into a functional of the electron density". *Phys. Rev. B* **37** (2): 785-789.
20. S. H. Vosko; L. Wilk; M. Nusair (1980). "Accurate spin-dependent electron liquid correlation energies for local spin density calculations: a critical analysis". *Can. J. Phys.* **58** (8): 1200-1211.
21. Ditchfield, R; Hehre, W.J; Pople, J. A. (1971). "Self-Consistent Molecular-Studies of Organic Molecules". *J. Chem. Phys.* **54** (2): 724-728.
22. Rick A. Kendall and Herbert A. Früchtl. The impact of the resolution of the identity approximate integral method on modern ab initio algorithm development. *Theoretical Chemistry Accounts: Theory, Computation, and Modeling* (*Theoretica Chimica Acta*), 97(1-4):158-163, October 1997.
23. Volkov, T. Koritsanszky, M. Chodkiewicz, H. F. King, on the basis-set dependence of local and integrated electron density properties: Application of a new computer program for quantum-chemical density analysis, *J. Comp. Chem.* 30, 1379-1391 (2009).
24. AIMAll (Version 12.11.09), Todd A. Keith, TK Grist mill Software, Overland Park KS, USA, 2012, URL: <http://aim.tkgristmill.com>.
25. R. F.W. Bader, 'Atoms in Molecules – A Quantum Theory', Oxford University Press, Oxford, 1990.

26. P. L. A. Popelier, *Sci. Comp. World*, 1999, **45**, 26.
27. Y. Aray and R. F.W. Bader, *Surface Sci.*, 1996, **351**, 233.
28. P.F.Zou and R. F.W. Bader, *Acta Cryat. A*, 1994, **50**, 714.
29. P.L.A. Popeileir and R. F. W Bader, *Chem. Phy. Lett.*, 1992, **189**, 542.
30. P.L.A. Popeileir and G. Logothetis, *J. Organomet. Chem.*, 1998, **555**, 101.
31. P.J. MacDougall, G. J. Schrobilgen and R. F. W. Bader, *Inorg. Chem.*, 1989, **28**, 763.
32. R. F. W. Bader and C. Chang, *J. Am. Chem. Soc.*, 1989, **93**, 2946
33. I. Bytheway, G. B. Bacskay and N. S. Hush, *J. Phys. Chem.*, 1996, **100**, 6023.
34. R. F. W. Bader and D. A. Leagare, *Can. J.Chem.*, 1992, **70**, 657
35. J. P. Ritchie and S. M. Bachrach, *J. Am. Chem. Soc.*, 1987, **109**, 5909.
36. .K. B. Wiberg, C. M. Breneman, *J. Am. Chem. Soc.* 1990, 112, 8765.
37. .M. Messerschmidt, A. Wagner, M. W. Wong, P. Luger, *J. Am. Chem. So*
c. 2002, 124, 732
38. Experimental electron density, determination of unconventionally bonded boron; Dissertation; Göttingen 2009
39. R. F. W. Bader, *Atoms in Molecules - A Quantum Theory*, Oxford Unive
rsity Press, New York, 1990.
40. R. F. W. Bader, *J. Phys. Chem. A* 1998, 102, 7314.
41. H. Hopf, *Math. Ann.* 1927, 96, 209.
42. K. Collard, G. G. Hall, *Int. J. Quantum Chem.* 1977, 12, 623.

43. T.H. Tang, R. F. W. Bader, P. J. MacDougall, *Inorg. Chem.* 1985, 24, 2047.
44. R. J. Gillespie, *Molecular Geometry*, Reinhold Van Nostrand, London, 1972.
45. R. J. Gillespie, I. Hargittai in *The VSEPR Model of Molecular Geometry in The VSEPR Model of Molecular Geometry*, Allyn and Bacon, Boston, 1991.
46. I. Bytheway, R. J. Gillespie, T.H. Tang, R. F. W. Bader, *Inorg. Chem.* 1995, 34, 2407.
47. R. J. Gillespie, E. A. Robinson, *Angew. Chem.* 1996, 108, 539; *Angew. Chem. Int. Ed. Engl.* 1996, 35, 477.
48. P. J. MacDougall, M. B. Hall, R. F. W. Bader, J. R. Cheeseman, *Can. J. Chem.* 1989, 67, 1842
49. R. F. W. Bader, R. J. Gillespie, P. J. MacDougall, *Molecular Structure and Energetics* 1989, 11, 1.
50. R. F. W. Bader, S. Johnson, T.H. Tang, P. L. A. Popelier, *J. Phys. Chem.* 1996, 100, 15398.
51. *Chemical Bonding and Molecular Geometry* in *Chemical Bonding and Molecular Geometry* (Eds.: R. J. Gillespie, P. L. A. Popelier), Oxford University Press, New York, 2001.
52. J. Cheesemann, T.A. Keith, R.F.W. Bader, AIMpac Program Package, McMaster University, Hamilton (Ontario), 1992.

53. M. J. Frisch, G. W. Trucks, H. B. Schlegel, G. E. Scuseria, M. A. Robb, J. R. Cheeseman, G. Scalmani, V. Barone, B. Mennucci, G. A. Petersson, H. Nakatsuji, M. Caricato, X. Li, H. P. Hratchian, A. F. Izmaylov, J. Bloino, G. Zheng, J. L. Sonnenberg M. Hada, M. Ehara, K. Toyota, R. Fukuda, J. Hasegawa, M. Ishida, T. Nakajima, Y. Honda, O. Kitao, H. Nakai, T. Vreven, J. A. Montgomery, Jr., J. E. Peralta, F. Ogliaro, M. Bearpark, J. J. Heyd, E. Brothers, K. N. Kudin, V. N. Staroverov, R. Kobayashi, J. Normand, K. Raghavachari, A. Rendell, J. C. Burant, S. S. Iyengar, J. Tomasi, M. Cossi, N. Rega, J. M. Millam, M. Klene, J. E. Knox, J. B. Cross, V. Bakken, C. Adamo, J. Jaramillo, R. Gomperts, R. E. Stratmann, O. Yazyev, A. J. Austin, R. Cammi, C. Pomelli, J. W. Ochterski, R. L. Martin, K. Morokuma, V. G. Zakrzewski, G. A. Voth, P. Salvador, J. J. Dannenberg, S. Dapprich, A. D. Daniels, Ö. Farkas, J. B. Foresman, J. V. Ortiz, J. Cioslowski, and D. J. Fox, Gaussian09, Revision A.1, Wallingford: Gaussian, Inc., 2009.
54. P. W. Higgs, Vibrational modifications of the electron density in molecular crystals. II. Mean squares amplitudes of thermal motion, *Acta Cryst.* **8**, 99-104 (1955).
55. R. F. Stewart, Vibrational averaging of X-ray scattering intensities, *Isr. J. Chem.* **16**, 137-143 (1997)
56. W. C. Price. *J. Chem. Phys.* **15**, 615 (1947); **16**, 894 (1948).
57. <http://en.wikipedia.org/wiki/Diborane>.

58. Wade, K. *Chem. Commun.* 1971, 792-793.
59. A. Tippe and W. C. Hamilton, *Inorg. Chem.*, 8, 464 (1969).
60. (a) R. Schaeffer, J. N. Shoolery, and R. Jones, *J. Amer. Chem. Soc.*, 79, 4606 (1957); 80, 2760 (1958); (b) T. Shapiro, M. Lustig, and R. E. Williams, *ibid.*, 81, 838 (1959); (c) J. A. Dupont and M. F. Hawthorne, *ibid.*, 84, 1804 (1962); (d) R. L. Pilling, F. N. Tebbe, M. F. Hawthorne, and E. A. Pier, *ibid.*, 86, 402 (1964); (e) P. C. Keller, D. MacLean, and R. Schaeffer, *Chem. Commun.*, 204 (1964).
61. T. Onak and D. Marynick, *Trans. Faraday Soc.*, 66, 1843 (1970).
62. R. F. W. Bader, T. T. Nguyen-Dang, and Y. Tal. *Rep. Prog. Phys.* 44, 893 (1981).
63. R. E. Dickerson, P.J. Wheatley, P.A. Howell, and W.N. Lipscomb. *J Chem. Phys.*, 27, 200 (1957). The crystal and molecular structure of B₉H₁₅.
64. K. Eriks, W.N. Lipscomb, and R. Schaeffer, *J. Chem. Phys.*, 22, 754 (1954). The boron arrangement in a B₆ hydride.
65. F.L. Hirshfeld, K. Eriks, R.E. Dickerson, E. L. Lippert, Jr., and W.N. Lipscomb, *J. Chem. Phys.*, 28, 56 (1958). Molecular and crystal structure of B₆H₁₀.
66. Bühl and Schleyer *J. Am. Chem. Soc.*, Vol. 114, No. 2, 1992

APPENDICES

APPENDIX A: ADDITIONAL TABLES

Table A 1: B_2H_6 , D_{2h} , $E_e = -52.8414$ au. (Atomic coordinates are in atomic units).

Atoms	X	Y	Z
B1	0.000000	-0.000000	-1.661330
H2	+0.000001	-1.840279	0.000000
H3	+0.000000	+1.840279	0.000000
B4	0.000000	-0.000000	+1.661330
H5	+1.955470	+0.000000	+2.752934
H6	-1.955471	-0.000000	+2.752933
H7	+1.955470	+0.000000	-2.752934
H8	-1.955471	-0.000000	-2.752933

Table A 2: B_5H_9 , C_{4v} , $E_e(A) = -128.632$ au. (Atomic coordinates are in atomic units)

Atoms	X	Y	Z
B1	0.000000	+2.396261	-0.271967
B2	0.000000	0.000000	+1.839846
B3	0.000000	-2.396261	-0.271967
B4	-2.396261	0.000000	-0.271967
B5	+2.396261	0.000000	-0.271967
H6	+1.808043	+1.808043	-1.952787
H7	-1.808043	+1.808043	-1.952787
H8	+1.808043	-1.808043	-1.952787
H9	-1.808043	-1.808043	-1.952787
H10	0.000000	+4.608383	-0.003681
H11	+4.608383	0.000000	-0.003681
H12	0.000000	0.000000	+4.065986
H13	-4.608383	0.000000	-0.003681
H14	0.000000	-4.608383	-0.003681

Table A 3: B_6H_{10} , C_s , $E_e(A) = -153.9$ au. (Atomic coordinates are in atomic units).

Atoms	X	Y	Z
B1	-0.000057	-2.787757	+0.144619
B2	+0.000001	+0.004442	-1.608557
H3	-0.000104	-4.881979	-0.615851
B4	+2.672363	-0.697086	+0.216574
B5	-2.672388	-0.696985	+0.216578
H6	+1.791058	-2.556068	+1.795879
H7	-1.791160	-2.555983	+1.795885
H8	+0.000001	-0.007755	-3.839738
B9	+1.544166	+2.384107	+0.307006
B10	-1.544072	+2.384167	+0.307003
H11	+4.728756	-1.378840	-0.306986
H12	-4.728808	-1.378651	-0.306989
H13	+2.595077	+0.955361	+2.092277
H14	-2.595042	+0.955467	+2.092275
H15	+3.016107	+3.946945	-0.311428
H16	-3.015950	+3.947062	-0.311436

Table A 4: B_6H_{14} , C_s , $E_e(A) = -257.081$ au. (Atomic coordinates are in atomic units).

Atoms	X	Y	Z
B1	+3.386861	+0.000010	+1.852120
B2	+1.880029	+2.681194	+0.466865
B3	+1.880037	-2.681187	+0.466873
B4	+2.828115	+0.000013	-1.351273
B5	-0.000003	-1.680352	-2.054465
B6	-0.000015	+1.680356	-2.054464
B7	-2.828129	-0.000004	-1.351261
B8	-1.880024	-2.681190	+0.466886
B9	-1.880037	+2.681182	+0.466891
B10	-3.386857	-0.000007	+1.852124

Table A4 (cont.)

Atoms	X	Y	Z
H11	+1.944886	+1.827930	+2.801679
H12	+5.299847	-0.000032	+2.996460
H13	-1.944795	+1.827970	+2.801599
H14	-1.944805	-1.827986	+2.801598
H15	+4.527781	+0.000011	-2.795144
H16	-0.000005	-3.058973	-3.812664
H17	+2.890793	+4.666775	+0.553686
H18	+1.944838	-1.827989	+2.801591
H19	+2.890832	-4.666755	+0.553625
H20	-2.890805	-4.666766	+0.553659
H21	-4.527800	-0.000004	-2.795126
H22	-5.299799	-0.000007	+2.996535
H23	-2.890823	+4.666755	+0.553669
H24	-0.000026	+3.058993	-3.812652

Table A 5: B_4H_{10} , C_{2v} , $E_e = -104.525$ au. (Atomic coordinates are in atomic units).

Atoms	X	Y	Z
B1	-1.621289	0.000000	-0.871756
B2	+1.621289	0.000000	-0.871756
B3	0.000000	+2.660712	+0.734493
B4	0.000000	-2.660712	+0.734493
H5	-2.590040	0.000000	-2.880294
H6	+2.590040	0.000000	-2.880294
H7	-2.484436	+1.733970	+0.495884
H8	-2.484436	-1.733970	+0.495884
H9	+2.484436	-1.733970	+0.495884
H10	+2.484436	+1.733970	+0.495884
H11	0.000000	+2.732537	+2.983003
H12	0.000000	+4.587092	-0.408163
H13	0.000000	-2.732537	+2.983003
H14	0.000000	-4.587092	-0.408163

Table A 6: $B_6H_6^{2-}$, O_h , $E_e(A) = -152.736$ au. (Atomic coordinates are in atomic units).

Name	X	Y	Z
B1	0.000000	0.000000	+2.314931
B2	0.000000	+2.314931	0.000000
B3	-2.314931	0.000000	0.000000
B4	0.000000	-2.314931	0.000000
B5	+2.314931	0.000000	0.000000
B6	0.000000	0.000000	-2.314931
H7	0.000000	0.000000	-4.605507
H8	0.000000	0.000000	+4.605507
H9	0.000000	+4.605507	0.000000
H10	-4.605507	0.000000	0.000000
H11	+4.605507	0.000000	0.000000
H12	0.000000	-4.605507	0.000000